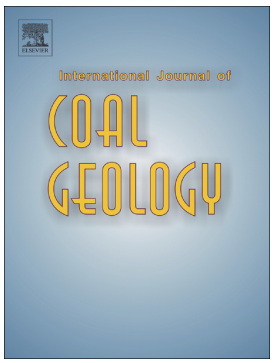

Matrix permeability anisotropy of organic-rich marine shales and its geological implications: Experimental measurements and microscopic analyses

Yong Ma, Huiting Hu, Zhejun Pan, Ningning Zhong, Fujie Jiang, Chengyu Yang, Jianbin Ma, Binhao Feng

PII: S0166-5162(24)00227-1

DOI: https://doi.org/10.1016/j.coal.2024.104670

Reference: COGEL 104670

To appear in: *International Journal of Coal Geology*

Received date: 25 July 2024

Revised date: 13 November 2024

Accepted date: 9 December 2024

Please cite this article as: Y. Ma, H. Hu, Z. Pan, et al., Matrix permeability anisotropy of organic-rich marine shales and its geological implications: Experimental measurements and microscopic analyses, *International Journal of Coal Geology* (2024), https://doi.org/10.1016/j.coal.2024.104670

Matrix permeability anisotropy of organic-rich marine shales and its geological implications: experimental measurements and microscopic analyses

Yong Ma[1], Huiting Hu[1], Zhejun Pan[2], Ningning Zhong[1], Fujie Jiang[1], Chengyu Yang[1], Jianbin Ma[1], Binhao Feng[1]

[1]State Key Laboratory of Petroleum Resources and Engineering, China University of Petroleum (Beijing), Fuxue Road No. 18, Changping, Beijing 102200, China

[2]State Key Laboratory of Continental Shale Oil, Northeast Petroleum University, Daqing, Heilongjiang 163318, China

Abstract

Due to the presence of natural and/or preparation-related fractures, the anisotropy of the matrix permeability of shales is usually difficult to characterize. In this study, we used X-ray micro-computed tomography (XRμCT) imaging to select samples from the Lower Cambrian and Upper Ordovician Wufeng Formation and the Lower Silurian Longmaxi Formation of the Upper Yangtze Platform, China, showing no natural or artificial fractures. From these samples, cubic specimens were prepared with a wire saw and then re-inspected for fractures. Using a specially developed sample holder, the matrix permeability of these specimens were measured in the three principal directions using the pulse decay method with N_2 as the flowing fluid. To analyze the microscopic lithological and structural controls on shale matrix permeability anisotropy, we employed a combined methodology using thin sections, focused ion beam-scanning electron microscopy (FIB-SEM), and permeability simulation.

The matrix permeability of the 15 shale samples ranged from 19.6 to 189.4 nD ($19.6 – 189.4 \times 10^{-21}$ m^2) parallel to bedding and from 2.4 to 24.7 nD ($2.4 – 24.7 \times 10^{-21}$ m^2) perpendicular to bedding, at a constant confining pressure of 1500 psi (10.3 MPa). Tectonic stress resulting from structural deformation leads to the deformation of OM pores within solid bitumen, which is the main factor controlling the matrix permeability. The ratio of the matrix permeability coefficients parallel and perpendicular to bedding (k_x/k_z) varied from 3.4 to 29.6, primarily due to cleavage zones along the bedding-parallel platy mica and clay altered from mica. The matrix permeability ratio in the two orthogonal horizontal directions (k_x/k_y) typically did not exceed a value of 2, but for samples with oriented graptolites and siltstone layers ratios as high as 2.9 and 2.3, respectively, were observed. The microfractures between graptolite and minerals, together with the elongated pores within the graptolites, enhance the permeability

and facilitate gas flow along the bedding planes. The higher proportion of brittle minerals in siltstone renders it more prone to cracking compared to shale, which causes the anisotropy in the parallel-to-bedding directions.

For three shales from the strongly deformed northeast Chongqing with high-angle fractures parallel to the lamination, permeability parallel to bedding varied between 627.2 and 6820.3 nD, while permeability perpendicular to bedding ranged between 11.3 and 27.8 nD. The presence of microfracture parallel to the lamination in three shale samples resulted in a permeability higher by factors of 34 to 348 than the matrix permeability, leading to a higher anisotropy ratio between both horizontal and vertical directions.

Keywords: Matrix permeability, permeability anisotropy, gas shale, tectonic deformation, platy mica, graptolite layers

Highlights

1. Matrix permeability anisotropy in shales was determined on cubic specimens
2. Deformation of OM pores by tectonic stress controls horizontal matrix permeability.
3. Platy mica causes permeability anisotropy parallel and perpendicular to bedding
4. The orientation of graptolite and siltstone layers increases the layer-parallel permeability anisotropy
5. Gas flow along micro-fractures exceeds matrix flow by one to two orders of magnitude

1. Introduction

Shale is a fine-grained clastic sedimentary rock that serves as both a caprock of conventional oil and gas and a storage reservoir for shale gas/oil, CO_2 (Armitage et al., 2011; Hou et al., 2024; Li et al., 2024) and radioactive waste (Wenk et al, 2008; Sasaki and Rutqvist, 2024) due to its ultra-low permeability. Transport of fluid within shale is controlled by the interconnectivity of mesopores and macropores within the shale matrix and the natural or hydraulic fracture systems (Ghanizadeh et al., 2014a, b). Given the significantly lower permeability of the shale matrix compared to the fracture system, hydraulic fracturing induced fractures are indispensable and regarded as the primary pathways for gas production in commercial shale gas operations. Some previous studies have indicated that despite the presence of hydraulic fractures, fluid transport within the matrix, however, is the primary factor limiting long-term gas production in shale gas plays (Boyer et al., 2006; Bustin and Bustin, 2012; Patzek et al., 2013). The significance of fluid transport in the shale matrix has been highlighted in previous shale gas reservoir

models (Luffel et al., 1993; Kalantari-Dahaghi, 2011; Bustin and Bustin, 2012). Several mathematical models have also been developed to characterize fluid transport phenomena within the shale matrix (Fathi and Akkutlu, 2009; Javadpour, 2009; Cipolla et al., 2010; Shi et al., 2021). Shales exhibit weaknesses parallel to bedding, besides natural fractures along bedding, sampling disturbances (e.g., coring) can readily introduce microfractures along the bedding planes (Gale and Holder, 2010). The presence of any fractures will significantly influence flow behavior, thereby hindering the proper characterization of matrix permeability. Therefore, very few studies have experimentally investigated the fluid flow mechanisms in the matrix of organic-rich shales mainly due to problems associated with the availability and preparation of appropriate shale samples.

Shale permeability is consistently higher in gas flows parallel to the laminations compared to flows perpendicular to the laminations, with anisotropic values ranging from 3.1 to 6800 (Pathi et al., 2008; Metwally and Sondergeld., 2011; Chalmers et al., 2012; Ghanizadeh et al., 2014a; Bhandari et al., 2015; Pan et al., 2015; Ma et al., 2016). Previous studies have attributed permeability anisotropy in shales to the microstructure (bedding/lamination planes), pre-existing microfractures, and the orientation of clay-rich fabric and pores/cracks along a preferential direction, resulting from sedimentation, compaction and diagenesis (Georgi et al., 2002; Kwon et al., 2004; Pathi, 2008; Metwally and Sondergeld, 2011; Kanitpanyacharoen et al., 2012; Ghanizadeh et al., 2014b; Bhandari et al., 2015; Lyu et al., 2024). Additionally, fractures formed by tectonic stress often exhibit directionality, leading to permeability anisotropy in two horizontal directions (Ma et al., 2016; Zhu et al., 2019). However, anisotropy of matrix permeability between parallel to bedding directions remains poorly understood. A key issue is how to accurately characterize the matrix permeability anisotropy.

Although permeability anisotropy is a well-known phenomenon in petrophysics, it is under-represented in experimental studies. Laboratory measurements of shale anisotropic permeability usually involve horizontally or vertically drilled plugs from cores (Chalmers et al., 2012; Ghanizadeh et al., 2014a, b; Bhandari et al., 2015; Mukherjee and Vishal, 2023). However, this method may not accurately represent the actual permeability anisotropy of highly heterogeneous shales (Chen et al., 2014; Pan et al., 2015), as the pore and microfracture systems can vary significantly between plugs. Pan et al. (2015) first used cubic specimens embedded in a 3D-printed membrane to measure the permeability coefficients of the same sample for rocks in the three principal directions. This method has since been widely used to characterize the permeability anisotropy of rocks (Ma et al., 2016; Zhao et al., 2022), allowing for the assessment of permeability anisotropy and its relation to the pore and microfracture system of sedimentary rocks.

In this work, we present the results of permeability measurements on 18 shale samples performed on cubic specimens in the three principal directions. The samples are from the Lower Cambrian and Upper Ordovician Wufeng Formation and the Lower Silurian Longmaxi Formation from three tectonic deformation regions on the east in the upper Yangtze Platform. Special care was taken to select matrix samples without fractures. The samples were characterized by petrographic and mineralogical methods. Finally, the geological controls on shale matrix permeability anisotropy were analyzed.

2. Sample origins and Experimental methods

2.1. Geological setting

A total of eighty shale core samples were collected from five shale gas wells located on the Upper Yangtze Platform, which tectonically comprises the western part of the Yangtze Platform in South China and is surrounded by the Longmenshan orogen in the west and the Qinling-Dabie orogen in the north (Meng et al, 2005) (Fig.1 and 2). The regional geological setting of NE and SE Chongqing has been described in detail in a previous study (Ma et al., 2020). The NE Chongqing area is tectonically located in the Dabasha arc-like thrustfold belt, which was formed during the collision orogenesis between the South Qinling and the Yangtze block in the Late Triassic. Here tight folds and thrust faults are common and the stratigraphic dip of the Lower Cambrian shales is 30–80° (Fig.1a and b) referred to as a strongly deformed zone (Zhang et al., 2001; Ma et al., 2020). The SE Chongqing area, outside of the Sichuan Basin, tectonically appears as syncline in an NW-SE direction (Fig. 1c) (Ma et al., 2020). The layers in this area are nearly horizontal and can be reasonably considered as a non-deformed zone. The Central Hunan area is tectonically located at the section where the direction of strike of the Jiangnan-Xuefeng Uplift arc structure transitions from NNE to NE-ENE, with the main part belonging to the Xuefeng Mountain basement fold-thrust belt (Fig. 1d, cross section C-C' in Fig. 1). This area is characterized by well-developed folds and oblique thrust faults, with numerous faults roughly parallel to the folds within the NE-NNE structural zone, and the stratigraphic dip of the Lower Cambrian shales range from15 to 50° (Li et al., 2022). The Central Hunan area is referred to as the moderately deformed zone. Therefore, based on the intensity of structural deformation, the deformation is strongest in NE Chongqing (A-A'), moderate in central Hunan (C-C'), and weakest in SE Chongqing (B-B'). Both the Lower Cambrian and Upper Ordovician Wufeng -Lower Silurian Longmaxi shales are organic rich shales deposited in a deep shelf environment (Zhao et al., 2016). Sample numbers, well names, series/formations, and depths are listed in

Table1.

2.2. Sample preparation

Freshly drilled shale core samples were initially used for canister desorption tests using the method described by Ma et al. (2015) to determine the gas content at the well site. Then, from shale cores showing no natural or artificial fractures were selected for micro-CT inspection cross and vertical section (Fig.3a, b and c). For core samples with microfractures detected by micro-CT (with a resolution of 30 μm), we selected areas without microfractures, as indicated by the red boxes in (Fig. 3b and c), for preparation of cubic samples. A digital control wire-electrode cutting was used to cut the shale cubes with lengths of 20± 0.1mm vertically (Fig. 3d) . Air, instead of water, was used to cool the wire saw to avoid any reaction between water and shale. The cubic shale samples were re-inspected using micro-CT to check for any artificial fractures (with a resolution of 9.89 μm)that may have formed during the wire saw cutting (Fig. 3e). Cubic shale samples showing no detectable fractures were used for matrix permeability measurements. The three samples from NE Chongqing with fractures along bedding were also used to compare matrix and fracture permeability. Before porosity and permeability measurements, the cubic samples were dried at 35°C under vacuum until their mass remained constant for at least 24 hours.

From the offcuts of the shale cubes in the two horizontal (x and y) and the vertical (z) directions, material was taken for the preparation of thin sections and for scanning electron microscopy (SEM). The rest of the offcuts was crushed for TOC and X-ray diffraction analyses.

2.3. Permeability measurement

Permeability measurements on the cubic samples were performed on a CoreLab PDP-200 permeameter, which uses the pulse-decay permeability (PDP) method. This is a proven rapid and accurate procedure for the determination of permeability coefficients down to the nanoDarcy (nD) range (Mukherjee and Vishal, 2023; 1 nD ~ 10^{-21} m^2). This method, originally described by Brace et al. (1968), and refined by Dicker and Smits (1988) and Jones (1997), uses the general solution of the pressure difference between upstream and downstream reservoir as a function of time to determine the permeability coefficients.

The cubic samples were placed into a 3D-printed polymer membrane with an outer diameter of 38.1mm (1.5 inch) (Fig.3f). Then the membrane with the installed cubic sample was placed inside the measuring cell, with upstream and downstream compartments of known volume, and equipped with pressure transducers. A confining pressure of 1500 psi (10.34MPa) and a pore pressure of 1100 psi (7.58MPa)

with a ΔP of 30 psi (0.21 MPa) were used for all samples with nitrogen (N_2) as the test gas in all experiments

The entire measuring device was placed in a temperature-regulated glass protection box with the temperature kept constant at 20°C. The membrane sample holder for the cubic shale samples was leak-tested before use by installing a steel cube with the same dimensions as the shale samples (Fig. 3e). As shown in Fig. 4a, the differential pressure in the upstream and downstream remained unchanged for 14 hours, demonstrating that no flow occurred across the membrane and that the sample was well sealed.

The permeability measurements were started by applying an instantaneous differential pressure (ΔP) between the upstream and the downstream compartment and recording the pressures in both compartments over time. After a certain period, the pressure difference between the upstream and downstream reservoirs approaches zero (Fig. 4b). The recorded decay in pressure difference (decay curves, cv Fig. 4) were evaluated using the PDP-200 software to obtain the permeability coefficients.

For each cubic sample, two orthogonal horizontal permeabilities were measured first, followed by vertical permeability. After each measurement, the sample was re-oriented and placed in the triaxial cell to assess permeability along each directional axis (Pan et al., 2015).

It is known that shale permeability decreases with increasing confining pressure and mean gas pressure (Chalmers et al., 2012; Ghanizadeh et al., 2014a; 2014b). While our measurements do not reflect permeability under reservoir conditions (where, assuming a hydrostatic pressure gradient, pressures range from 797 psi [5.5 MPa] to 2915 psi [20.1 MPa]), the experiments were conducted under consistent conditions. Therefore, the comparison of permeability anisotropy among different samples remains meaningful.

2.4. X-ray micro-CT measurement and interpretation technique

X-ray micro-CT can observe the internal structure of rock samples (Liu et al., 2023) and a Sanying nanoVoxel-3000 was used in this study for both the core samples and cubic specimens. Typical micro-CT image cross section does not exceed 4000 voxels in each direction. Thus, the size of the investigated core samples scales linearly decrease with the resolution (Bazaikin et al., 2017). Two-dimensional CT scan images were collected for core samples in three directions to characterize the natural fractures with a resolution of 30 μm (Fig. 3b and c). Cubic specimens were scanned and reconstructed in three dimensional to inspect the microfractures with a resolution of 9.89 μm. The 3-D CT data was imported into Avizo 9.0.1 imaging software to generate a 3D rendering of the shale. The visual microfractures can

be extracted based on the images grey value histogram.

2.5. QEMSCAN, FIB-SEM reconstruction

The opposite sections of the cubic shale were initially mechanically polished and then milled by the argon-ion-beam. Sample coated with carbon were inserted into a Zeiss Merlin field emission scanning electron microscopy (FE-SEM) for imaging and Quantitative Evaluation of Minerals by Scanning electron microscopy (QEMSCAN) analyses. The FE-SEM equipped with a Amics software that can convert the elemental composition in combination with back-scattered electron (BSE) and X-ray count rate information into mineral phases. The QEMSCAN results can provide quantitative analyses of bulk mineralogy, textural properties, particle, and mineral grain sizes (Fu et al., 2023). The pixel resolution of the images in this study is 1μm.

The SEM samples were then inserted into a Zeiss Crossbeam 540 FIB-SEM for FIB milling and SEM imaging sequentially. The experimental workflow was same as in a previous work described in Ma et al. (2015), with an exception that the angle of the ion beam and electron beam are adjusted from 52° to 54°. Finally, a sequence of more than 800 SEM images with a resolution of 10 nm are achieved. The FIB-SEM data were also imported into Avizo 9.0.1 imaging software for 3-D rendering of shale structure. Subsequent Quantitative analyses of organic matter and pore networks were conducted by assigning gray-scale values and setting thresholds to segment the features.

2.6. Absolute permeability simulations

Absolute permeability, defined as the ability of a porous medium to transmit a single-phase fluid, is an intrinsic property that is independent of external conditions. It can vary with the direction of flow and will henceforth be referred to simply as permeability. After generating a 3-D rendering of pore networks using FIB-SEM images, the absolute permeability of the interconnected pore network can be quantified using Avizo software by applying a finite element image-based simulation method (Peng et al., 2014; Avizo, 2018; Callow et al., 2018; 2020). In this method, each voxel corresponds to a mesh element, eliminating the need for an additional meshing process (Callow et al., 2020).

In Avizo, it is assumed that the pore fluid behaves as a steady-state, incompressible Newtonian fluid under laminar flow conditions (low Reynolds number). The velocity of the simulated fluid flow through the pore network can be calculated by solving the Stokes flow equation:

$$\begin{cases} \mu\nabla^2 v - \nabla p = 0 \\ \nabla \cdot v = 0 \end{cases} \quad (1)$$

where, μ is the dynamic viscosity of the flowing fluid, ∇^2 is the Laplacian operator, v is the fluid velocity, p is the simulated fluid pressure.

The boundary conditions for the simulation include a no-slip surface at the pore-solid interface. Additionally, a solid plane, one voxel thick, is placed parallel to the main flow direction to maintain the fluid within a closed system. An experimental configuration is applied to the faces perpendicular to the flow direction to create a quasi-static pressure state and ensure fluid flows through the entire cross-sectional input and output areas. To obtain reliable and repeatable permeability values, the Stokes-flow simulations must converge with a low tolerance error. In the Avizo fluid simulation, a convergence coefficient of 10^{-5} was employed.

Once eq. (1) is solved through convergence of the simulation and the volumetric flow rate (Q) is calculated, the permeability (k) can be estimated using Darcy's law:

$$k = \frac{\mu L Q}{\Delta P A} \quad (2)$$

where k is the absolute permeability (m^2), μ is the dynamic viscosity of the flowing fluid (Pa.s), L is the sample length in the flow direction (m), Q is the volumetric flow rate (m^3/s), ΔP is the pressure difference across the sample (Pa), and A is the cross sectional area (m^2). In this study, water was assumed as the pore fluid, with upstream and downstream fluid pressures for the pore network calculations set to 1.3×10^5 Pa and 1.0×10^5 Pa, respectively.

2.7. Porosity, pore-size distribution (PSD) and surface area

The porosity of the cubic samples was determined using a CoreLab UltraPore 300 helium pycnometer. The dried cubic specimens were first measured for their overall dimensions to calculate bulk volumes (V_b). They were then placed in a matrix cup with a diameter of 1.5 inches. The UltraPore 300 pycnometer applies Boyle's Law to determine the grain volume (V_g) by measuring the expansion of a known mass of helium at a pressure of 200 psi (1.38 MPa) into the calibrated matrix cup. Porosity (∅) can be calculated using the following equation:

$$\emptyset = 1 - \frac{V_g}{V_b} \quad (3)$$

Repeated measurements showed an accuracy of less than 5%.

Specific surface areas were determined by N_2 and CO_2 adsorption with a Micromeritics ASAP 2020^M apparatus using the same experimental conditions described previously (Ma et al., 2020). The N_2 adsorption was measured at 77.35 K up to a pressure of 101.3 kPa with relative pressures (P/P_0) ranging from 0.01 to 0.997. The five-point Brunauer-Emmett-Teller (BET) method and the Barrett-Joyer-Halenda (BJH) method were used to calculate the surface area and pore volume of pores (2–200 nm), respectively, from the N_2 adsorption data. For CO_2 adsorption, the experimental temperature was maintained at 273 K, with relative pressures (P/P_0) ranging from 0.0003 to 0.023. The density functional theory (DFT) method was used for the determination of specific surface areas and specific volumes of the micropores (0–2 nm).

2.8. Total organic carbon (TOC) content and vitrinite reflectance

The total organic carbon (TOC) content (wt. %) was determined using a Leco-CS230 carbon and sulfur analyzer, with an analytical precision of ± 0.5%. Powdered samples (<200 mesh) were pretreated with 10 wt% HCl to remove carbonate minerals, followed by washing with distilled water to neutralize the solid residues. The solid residues were then dried in an oven at 80°C before TOC analysis.

Shale blocks, cut perpendicular to the bedding direction, were embedded in a cold-setting epoxy-resin mixture. The blocks were then ground and polished prior to microscopy. The reflectance of the solid bitumen was measured using a Leica MPV-III microphotometer, with at least 30 measurement points taken for each sample. The random bitumen reflectance (R_b) was converted to equivalent vitrinite reflectance ($EqVR_o$) using Jacob's (1989) equation:

$$EqVR_o = 0.618R_b + 0.4 \quad (2)$$

2.9. X-ray diffraction (XRD)

Mineral phase identification for selected samples was performed using X-ray diffraction (XRD) analysis with a Bruker D2 Discover powder diffractometer. Approximately 10 g of crushed sample (<200 mesh) was mixed with ethanol, hand-ground, and smear-mounted onto glass slides. A normal-focus Cu X-ray tube was used at 40 kV and 40 mA. No internal standard was applied in the XRD analysis, and measurements were taken over a two-theta range of 5° to 80°. Semi-quantitative mineralogy was obtained by analyzing the spectra with Bruker AXS Topas® V7.0 software.

3. Results

3.1. Geochemical characteristics

As shown in Fig.2 and Table 1, the TOC content of the eighteen samples varies from 0.59 to 12.55% with an average value of 3.27%. The lower Cambrian shales exhibit a wider range of TOC content (0.72–12.55%) than the Upper Ordovician–Lower Silurian shales (0.59–2.05%). The thermal maturity of the studied shales ranges from 2.22 to 3.23% $EqVR_o$, indicating an over-mature source rock and a strongly diagenetically overprinted reservoir rock. Apart from the Lower Cambrian shales of YC2 well located in NE Chongqing, which exhibit relatively high desorbed gas contents (DGC) (0.59–1.03 m^3/t), the DGC of all other samples is generally below 0.6 m^3/t. The preservation of Lower Cambrian shale gas has been extensively discussed by Ma et al. (2015; 2020). In contrast, the poor performance of shale gas production in SE Chongqing and Central Hunan is influenced by a series of complex factors, including tectonic uplift, faults, and groundwater flow (Zhao et al., 2016).

3.2. Mineralogy and shale fabric

All shales are rich in quartz and feldspar, particularly quartz, with a mean value of 43.2%, ranging from 30.5 to 68.4% (Fig. 5 and Table 2). Plagioclase averages 8.6% with a range between zero and 19.2%, while K-feldspar is typically less than 5.7%. Carbonates, including calcite and dolomite, averaging 13.5% and ranging from 2.7 to 35.3%. Illite, mixed-layer illite-smectite (I/S), and chlorite are the major clay minerals, constituting the total clay content, which averages 28.1% and ranges from 12.3 to 52.9%. Pyrite averages 4.2% with a range between zero and 11.5%.

Shale lamination is found in all samples, reflecting compositional and textural variations. The dominant lithofacies are thin parallel laminated shale (Fig.6a-d), with some samples such as CY1-27 and YC8-54 comprising interlaminated fine to medium-grained siltstone (Fig.6a and b, Fig.7a-c). The preferred orientation of the long axes of ellipsoidal clasts, carbonate cementation, platy mica and clay result in a high degree of anisotropy for all shale samples (Fig.6 and 7). Graptolites are abundant in the Upper Ordovician Wufeng - Lower Silurian Longmaxi shales and exhibit both random and oriented arrangements (Fig.8), indicating in-situ deposition as well as alignment by water flow, respectively.

3.3 Porosity and pore structure

Porosity of the 18 shale samples measured by helium expansion ranges between 0.26 and 1.23% (Table 3). These values are slightly lower than the previously reported porosity range of 0.39% to 2.7%

for Lower Cambrian shales in NE and SE Chongqing (Cao et al., 2014; Ma et al., 2015, 2020; Sun et al., 2015). This relatively low porosity is likely due to the sample selection process, which specifically aimed to exclude samples with natural fractures.

The lower Cambrian Shuijingtuo shales from NE Chongqing, referred to as a strongly tectonically deformed zone, exhibit high-angle microfractures along the bedding as revealed by X-ray micro-CT reconstruction (Fig.9). These microfractures penetrate the cubic specimens in the two horizontal directions (x and y) of but not in the vertical direction (z) (Fig.9). These microfractures were most likely formed by the intense tectonic stress during the Qinling collision orogenesis. For the other 15 cubic specimens from the SE Chongqing and central Hunan, no visible microfractures larger than 9.89 μm were detected by X-ray micro-CT. These samples are therefore considered to represent the matrix pore system, and their measured permeability coefficients are considered to represent matrix permeability.

Detailed SEM observations of these over-matured shales reveal that strong diagenesis, including compaction and cementation, have made these fine-grained sedimentary rocks very tight (Fig.7). According to the classification by Loucks et al. (2012), matrix-related pores in shale, including mineral matrix pores, organic-matter (OM) pores, and fracture pores, which were identified in these samples.

(1) Mineral matrix pores: These include discrete pores between mineral grains (Fig.7e), bedding parallel micro-cracks between sub-horizontal platy-shaped minerals such as clay and mica and detrital grains contact (Fig. 7e), and elongated pores along cleavage of the platy clay and mica (Fig. 7e and f).

(2) Organic matter (OM) pores: Pores within the micrometer-sized solid bitumen are the dominant OM type in both shales (Fig.10), while pores associated with the graptolites form a negligible portion of OM type pores for the Wufeng-Longmaxi shales (Fig.8). OM pores within the solid bitumen exhibit varying features in the Lower Cambrian shales across different regions: pores are rounded or elliptical in SE Chongqing shales, become small and appear as pinhole pores in Central Hunan samples, and are not visible in NE Chongqing shales (Fig.10), corresponding to distinct structural deformation zones. Graptolites, preserved as flattened in the section perpendicular to bedding exhibit directionally arranged spindle-shaped pores between cortical fibrils, which are abundant within the graptolite. Additionally, microfractures are common at the contacts between graptolite and brittle minerals (Fig. 8).

(3) Microfractures: In addition to the micrometer-sized fractures associated along graptolites and mica, the matrix pore system also includes millimeter-sized fractures found in the siltstone (Fig.7a and b, Fig.11). These millimeter-sized fractures are directionally distributed, extending within the siltstone and disappearing within the shale. These microfractures were likely formed under tectonic stress, and the

difference in mineral rigidity in the siltstone versus the higher contents of plastic clay in the shale caused the microfractures to extend only within the siltstone (Zhu et al., 2019; Ma et al., 2020).

3.4 Shale permeability anisotropy

The shale matrix permeability values measured at a constant confining pressure of 1500 psi (10.3 MPa) in three directions are presented in Fig. 12 and Table 3. Shale matrix permeability parallel to bedding ranges from 19.6 to 189.4 nD and is thus significantly higher than the permeability perpendicular to bedding, which also varies within a smaller range of 2.4 to 24.7 nD. The Lower Cambrian Niutitang shales generally exhibit higher matrix permeability parallel to bedding (42.8-189.4 nD) than the shales in the Central Hunan samples (19.6-47.3 nD), while there is no significant difference in the matrix permeability in horizontal directions between the Longmaxi and Wufeng shales from SE Chongqing. The ratios of horizontal versus vertical permeability coefficients (k_x/k_z) vary from 3.5 to 29.6, evidencing a strong anisotropy. The ratio of matrix permeability in the two bedding-parallel directions (k_x/k_z) ranges from 1.1 to 2.9, and for most samples this ratio is below 2, with the exception of samples YC8-39 and CY1-27.

The Lower Cambrian Shuijing shales in NE Chongqing, with microfractures developed along the bedding (Fig.9), exhibit significantly higher horizontal permeability coefficients, ranging from 627.2 to 6820.3 nD (Fig.13, Table 3), than the samples without microfractures (Fig.12). However, the vertical permeability of these samples remains within a similar range, from 11.3 to 27.8 nD. Thus, the Lower Cambrian Shuijing shales in NE Chongqing have greater horizontal to vertical permeability ratios from 55.5 to 277.4. Furthermore, the permeability ratio between the two horizontal directions, specifically the x-direction to the y-direction, increases to a range of 2.6 to 4.4.

To quantitatively evaluate the permeability anisotropy of two important pore types within the shale matrix, permeability simulations were performed for three orthogonal directions based on 3D reconstruction of muscovite and solid bitumen using FIB-SEM data (Fig.14 and 15, Table 4). Muscovite appears as pseudo-hexagonal plates or flakes, with pores primarily distributed along its cleavage planes in a layered pattern (Fig.14a-c). The modelling results for a single muscovite grain indicate that permeability is isotropic along the cleavage planes and 6.9 times higher than permeability perpendicular to the cleavage direction (Fig.14a-c, Table 4), which causes the permeability anisotropy. The pores within solid bitumen exhibit no directional preference, and permeability modelling reveals negligible anisotropy, with permeability values being similar in all three principal directions (Fig.15, Table 4).

4.Discussion

4.1. Matrix permeability anisotropy (horizontal to vertical permeability ratio)

Our results show that the matrix permeability coefficients of these diagenetically altered shales vary from 19.6 to 189.4 nD in the horizontal direction and from 2.4 to 24.7 nD in the vertical direction (Fig. 12, Table 3). The presence of microfractures along bedding for the Lower Cambrian shales in NE Chongqing (Fig.9) results in an increase in horizontal permeability to 627.2 and 6820.3 nD, i.e. around 34 to 348 times higher than the horizontal matrix permeability (Fig. 13, Table 3). However, the vertical permeability coefficients of these shales range between 11.3 and 27.8 nD, which is similar to the vertical matrix permeability. This is mainly due to microfractures extending along horizontal directions, with no interconnected fractures in the vertical directions, despite the large dip angle of the Lower Cambrian shales in NE Chongqing (Fig.9). Fig.16 shows the measured anisotropic permeability of several shales using core plugs and cubic specimens at confining pressures from 3 to 15 MPa in this study and from the literature. For shales with horizontal permeability coefficients above 600 nD, visible fractures were observed (Pathi, 2008; Ma et al., 2016; this study). Therefore, based on the measured matrix permeability and limited data from previous studies, horizontal matrix permeability of shales is likely to range from 17 to 280 nD, as indicated by the shaded area in Fig.16. Besides the two shales with high vertical permeability (135 and 179 nD) that might contain microfractures (Pathi, 2008; Ghanizadeh et al., 2014a), the vertical permeability for shales, with or without fractures, ranges from 1.6 to 52.8 nD. This indicates that vertical permeability is generally very low, even for shales with well-developed fractures parallel to the lamination.

Permeability anisotropy of sedimentary rocks is defined as the ratio of the horizontal to vertical permeability coefficients. The horizontal permeability of shales is typically much higher than the vertical permeability, which results in high anisotropy values. The matrix permeability ratios (k_x/k_z) of the samples investigated in this study range from 3.5 to 29.6 (Table 3), which is similar to previous studies reporting values from 3.8 to 49.8 (Fig.16b). For shales with fractures parallel to the lamination this ratio increases to values between 55.5 and 277.4 (Table 3), which falls within the range 22.7 to 5583.4 as reported in previous studies (Fig.16b). This demonstrates that the presence of fractures parallel to the lamination significantly enhances horizontal permeability and is the primary cause of the pronounced permeability anisotropy in shales.

Besides the great enhancement of permeability anisotropy ratio by pre-existing fractures, geological controls on shale matrix permeability anisotropy can be attributed to lamination and preferred orientation

of minerals. Permeability anisotropy of homogeneous and nonlayered (isotropic) mudstones varies modestly between 1 and 4 (Clennell et al., 1999; Leroueil et al., 1999; Yang and Aplin, 1998; 2007; Adams et al., 2013). Considering the matrix permeability anisotropy of shales, which ranges from 3.5 to 49.8, this indicates that layering or lamination significantly increases shale permeability anisotropy. The SEM and QEMSCAN results in Fig. 7 and Fig. 10 show that intergranular pores between elliptic detrital minerals and the OM pores within solid bitumen do not have a preferential orientation and are isolated. Permeability modelling confirmed that OM pores within the solid bitumen are isotropic (Fig. 15). These intergranular and OM pores do not appear to enhance flow capacity in either the parallel or perpendicular directions to the bedding planes. The sub-horizontal platy-shaped muscovite or chlorite formed by alteration of biotite caused a sheet-like fabric in the shale. The microfractures along the mica and the elongated pores and cleavage along the preferred orientation of platy or chlorite act as good horizontal flow pathways (Fig.7). Permeability simulation of mica further confirmed that permeability along the cleavage planes is significantly higher than perpendicular to the cleavage (Fig.14). Therefore, platy muscovite or chlorite significantly enhance gas flow capacity parallel to the bedding planes while acting as barriers to gas flow perpendicular to the bedding planes, which is the main cause of matrix permeability anisotropy in shales (Fig.14).

4.2. Geological controls on matrix permeability in horizontal directions

As discussed above, both, our results and previous studies show that shale matrix permeability in horizontal directions varies within a small range with values from 19.6 to 189.4 nD and 17 to 280 nD, respectively (Fig.12, Fig.16, Table 3). Matrix permeability in horizontal directions does not show a significant correlation with TOC content, mineral composition, or the volume and surface area of micro- to macropores. Horizontal permeability of the Lower Cambrian shales exhibits significant regional differences; the shales in NE Chongqing with fractures parallel to the lamination show higher values (627.2–6820.3nD) than those in SE Chongqing (42.8–189.4nD), which in turn are higher than those in Central Hunan (19.6–47.3nD). This indicates the control of tectonic stress on shale microstructure and gas flow capacity.

Numerous studies have emphasized the critical role of OM-hosted pores for gas storage and flow in shales (Loucks et al., 2009; 2012; Mastalerz et al., 2018; Milliken et al., 2013, etc.). Detailed SEM observations have confirmed that OM porosity constitutes the primary pore network in the Lower Cambrian shales (Fig. 10). Pores in OM are thought to form as kerogen or solid bitumen converts to hydrocarbons, leading to the generation of liquids and gases that coalesce into bubbles (Mastalerz et al.,

2018; Milliken et al., 2013; Katz and Arango, 2018; Ma et al., 2020). Both, the Lower Cambrian shales in the eastern part of Upper Yangtze Platform were deposited on passive continental margins (Zhao et al., 2016), they are organic-rich and over-mature (Table 1). Therefore, OM pores within the solid bitumen in the Lower Cambrian shales in the three regions should be similar. When subjected to external mechanical stress, such as structural deformation, the plastic OM in shales is more likely to be affected, causing the collapse of meso-macro OM-hosted pores. In contrast, smaller pores (<10 nm) are generally considered resistant to mechanical compaction (Loucks et al., 2009; Katz and Arango, 2018; Zhu et al., 2019). According to the degree of structural deformation, the tectonic stress on the Lower Cambrian shales is strongest in NE Chongqing (strongly deformed zone), moderate in Central Hunan (moderately deformed zone), and weakest in SE Chongqing (non-deformed zone) (Fig.1). Correspondingly, pores within solid bitumen in the Lower Cambrian shales show significant variation in response to the intensity of structural deformation. In SE Chongqing, OM pores are rounded or elliptic; in Central Hunan, they become smaller and pinhole-shaped; and in NE Chongqing, they fade away and are not visible under the SEM (Fig.10). Apparently, the intense thrust nappe tectonics in the NE Chongqing area have not only led to the disappearance of organic matter pores in the shales but also resulted in the formation of numerous high-angle fractures parallel to the lamination (Fig.9).

In unconventional gas reservoirs, such as shale gas and coalbed methane, gas flow is characterized by a combination of desorption and diffusion within micropores (<2 nm) and mesopores (2–50 nm), along with Darcy flow through macropores (>50 nm) and the fracture network (Cui et al., 2009; Chalmers et al., 2012). Due to the decrease of OM pores in the Lower Cambrian shales, from SE Chongqing to Central Hunan and NE Chongqing (Fig.10), gas flow in the shale matrix pore system becomes increasingly difficult. Consequently, matrix permeability of the Lower Cambrian shales should decrease in this order. This is consistent with the measured matrix permeability of the Lower Cambrian shales in SE Chongqing and Central Hunan. However, the presence of fractures parallel to the lamination in NE Chongqing greatly enhances gas flow capacity, increasing permeability up to 350 times compared to matrix permeability (Table 3).

4.3 Matrix permeability anisotropy in two orthogonal horizontal directions

Unlike the well-studied permeability anisotropy in shales and mudstones, the matrix permeability of shales in two orthogonal have been studied seldomly, due to challenges in specimen preparation. Combined with cubic specimens and X-ray micro-CT, our results show that the ratio of two orthogonal

horizontal matrix permeability for most samples does not exceed 2, indicating a transversely isotropic medium. The exceptions are samples YC8-39 and CY1-27, which have permeability anisotropy ratios of 2.9 and 2.3, respectively (Fig. 12 and Table 3). It is suggested that the orientation of graptolites and the content of brittle mineral can cause this relatively high matrix permeability anisotropic ratio (>2) in horizontal directions.

As shown in Fig.8, graptolites in the Longmaxi shales exhibit anisotropic permeability depending on their orientation. For graptolites arranged in a preferred orientation in sample YC8-39, the permeability parallel to the long axis of the graptolites is 90.2 nD, which is three times larger than the permeability perpendicular to predominant orientation of the graptolites (30.7 nD) (Fig.8). Since the sizes of graptolites are in the centimeter range, there is an overlap with the numerous microfractures and the orientated spindle-shaped pores provided by the cortical fibrils of the graptolite. This significantly increases the gas flow capacity along the long axes of the graptolites (Fig. 8). This is further supported by the observation that for shale sample YC8-33 where graptolites are randomly orientated parallel to the bedding, the matrix permeability values in the two orthogonal horizontal directions are very similar (86.1 nD and 64.5 nD, Fig. 8b).

The presence of siltstone layers in shales causes heterogeneity not only in fabric but also in mineral brittleness. Siltstones contain a higher proportion of brittle minerals, such as quartz and carbonate, while to shales are rich in swelling clay minerals (Fig. 7 and Fig. 11). The higher composition of brittle minerals makes siltstones more prone to fracturing under tectonic stress and artificial hydraulic fracturing (Zeng et al., 2013; Ougier-Simonin et al., 2016). This is consistent with the development of microfractures in these shales, where high-angle microfractures, potentially controlled by tectonic stress, extend in siltstone and terminate at shale layers (Fig.7a-c; Fig.11). Sample CY1-27 has a higher percentage of siltstone (Fig. 11), as evidenced by a high content of brittle minerals, including quartz (44.9 wt.%) and dolomite (35 wt.%), and a low TOC content (0.72 wt.%) (Table1 and Table2). This causes microfractures to develop more extensively in the siltstone of sample CY1-27, greatly increasing permeability along the section with more microfractures affected by tectonic stress, due to their higher flow capacity compared to the shale matrix. Thus, sample CY1-27 has the highest matrix permeability in x-direction (189.4nD), where high angle microfractures are more developed, and it also has a high matrix permeability ratio of 2.3 in two orthogonal horizontal directions (Fig.11, Table 3).

Figure 17 schematically illustrates the geological controls on shale matrix permeability. Both, longitudinally oriented graptolites and detrital minerals exhibit a preferred orientation along their long

axis and thus determine the principal direction of water flow. This is especially true for overlapping graptolites in oriented arrangements (Fig. 8a), where microfractures in contact with graptolites, along with elongated pores within the graptolites, contribute to the flow channels and enhance permeability in in one principal direction. Mica, appearing as pseudo-hexagonal plates or flakes, does not exhibit preferential alignment determining the principal flow direction. Permeability simulations also confirm the isotropic permeability of mica parallel to its cleavage planes (Fig. 14, Table 4). Consequently, platy mica exhibits enhanced permeability in all horizontal directions but acts as a flow barrier perpendicular to its lamination. OM pores within solid bitumen, believed to form after hydrocarbon generation, show no directional preference. This is supported by permeability simulations of solid bitumen, indicating that OM pores enhance shale matrix permeability uniformly in all three directions. Siltstone layers, which contain more brittle minerals than shales, are more likely to develop microfractures under tectonic stress. These directionally aligned microfractures can greatly enhance permeability and create high permeability anisotropy in two orthogonal horizontal directions.

6. Conclusions

In this work, we combined XRμCT inspection and permeability measurements on cubic specimens to study the matrix permeability of a series of shales in three directions. The results represent a significant extension of the available database for comparison with previous studies. We then analyzed geological controls on matrix permeability anisotropy both between vertical and horizontal directions and two orthogonal horizontal directions based on 2D observations and 3D permeability simulations. The main conclusions drawn are as follows:

1. At a constant confining pressure of 1500 psi (10.34 MPa), matrix permeability in horizontal directions ranged from 19.6 to 189.4 nD and from 2.4 to 24.7 nD in vertical directions. The anisotropy ratio of horizontal vs. vertical permeability coefficients ranged from 3.5 to 29.6, and the ratio of permeability coefficients along the two orthogonal horizontal directions varied between 1.1 and 2.9. The presence of fractures parallel to the lamination greatly increases permeability along these directions by 32 to 348 times compared to matrix permeability, while it makes no difference for permeability across the lamination. The horizontal to vertical permeability anisotropy ratio for shales with bedding-parallel fractures increases to 55.5–277.4 and for the two orthogonal horizontal directions to values from 2.6 to 4.4.
2. Matrix permeability anisotropy in horizontal to vertical direction is mainly controlled by the preferred

orientation of platy mica or clay. Microfractures and cleavage along the bedding-parallel platy mica greatly increase the permeability in the horizontal directions, while these minerals act as barriers in the direction perpendicular to the cleavage. Additionally, due to the crystalline structure of pseudo-hexagonal plates or flakes, the permeability of mica along horizontal directions exhibits no discernible disparity.

3. Matrix permeability in horizontal directions is affected by the OM porosity, orientation of graptolites, and content of brittle minerals. For the Lower Cambrian shales in three regions with different structural deformation intensities, OM pores within solid bitumen decrease gradually with tectonic stress, causing the variation of matrix permeability correspondingly. Moreover, the OM pores within solid bitumen show isotropic permeability in three directions. The microfractures and elongated pores along graptolites greatly enhance gas flow capacity along the long axis of the graptolite, as shales with overlapped graptolite in oriented and random directions show distinctly different permeability. The siltstone layer contains a higher proportion of brittle minerals, making it more prone to produce fractures under tectonic stress. These fractures not only enhance matrix permeability but also cause permeability anisotropy in two orthogonal horizontal directions.

Acknowledgements

This work was supported by the National Natural Science Foundation of China Grant No. 42173030) and PetroChina Innovation Foundation (2018D-5007-0102). The authors express their gratitude to Dr. Bernhard Krooss (ORCID ID: https://orcid.org/0000-0001-7289-1533) for critical discussions and assistance with language editing.

References

Adams, A.L., Germaine, J.T., Flemings, P.B., Day-Stirrat, R.J., 2013. Stress induced permeability anisotropy of resedimented Boston Blue Clay. Water Resour. Res. 49, 1–11. https://doi.org/10.1002/wrcr.20470.

Armitage, P.J., Faulkner, D.R., Worden, R.H., Aplin, A.C., Butcher, A.R., Iliffe, J., 2011. Experimental measurement of, and controls on, permeability and permeability anisotropy of caprocks from the CO_2 storage project at the Krechba Field, Algeria. J. Geophys. Res. 116, B12208. https://doi.org/10.1029/2011JB008385.

Avizo, 2018. Avizo 3D Software User's Guide. FEI. https://www.fei.com/so ftware/avizo-user-guide/ (accessed 24.07.2024). in Version 9. 1–967.

Bazaikin, Y., Gurevich, B., Iglauer, S., Khachkova, T., Kolyukhin, D., Lebedev, M., Lisitsa, V., 2017. Effect of CT image size and resolution on the accuracy of rock property estimates. J. Gephys. Res. Solid Earth. 122 (5), 3635-3647. https:// doi.org/10.1002/2016JB013575.

Bhandari, A.R., Flemings, P.B., Polito, P.J., Cronin, M.B., Bryant, S.L., 2015. Anisotropy and stress dependence of permeability in the Barnett Shale. Transport Porous Med. 108, 393–411. https://doi.org/10.1007/s11242-015-0482-

0.

Boyer, C., Kieschnick, J., Suarez-Rivera, R., Lewis, R., Waters, G., 2006. Producing gas from its source. Oilfield Rev. 18, 36-49. https://doi.org/urn:nbn:se:uu:diva-19783.

Brace, W.F., Walsh, J.B., Frangos, W.T., 1968. Permeability of granite under high pressure. J. Geophys. Res. 73, 2225–2236. https://doi.org/10.1029/JB073I006P02225.

Bustin, A.M.M., Bustin, R.M., 2012. Importance of rock properties on the producibility of gas shales. Int. J. Coal Geol. 103, 132–147. https://doi.org/10.1016/j.coal.2012.04.012.

Callow, B., Falcon-Suarez, I., Ahmed, S., Matter, J., 2018. Assessing the carbon sequestration potential of basalt using X-ray micro-CT and rock mechanics, Int. J. Greenhouse Gas Con. 70, 146–156. https://doi.org/10.1016/j.ijggc.2017.12.008.

Callow, B., Falcon-Suarez, I., Marin-Moreno, H., Bull, J.M., Ahmed, S., 2020. Optimal X-ray micro-CT image based methods for porosity and permeability quantification in heterogeneous sandstones. Geophys. J. Int. 223 (2), 1210-1229. https://doi.org/10.1093/gji/ggaa321.

Cao, X.M., Yu, B.S., Li, X.T., Sun, M.D., Zhang, L., 2014. Reservoir characteristics and evaluation on logging of the Lower Cambrian gas shale in southeast Chongqing: a case study of Well Yuke 1 and Well Youke 1. Acta Pet. Sin. 35 (2), 233–244 (in Chinese with English abstract).

Chalmers, G.R., Ross, D.J., Bustin, R.M., 2012. Geological controls on matrix permeability of Devonian Gas Shales in the Horn River and Liard basins, northeastern British Columbia, Canada. Int. J. Coal Geol. 103, 120–131. https://doi.org/10.1016/j.coal.2012.05.006.

Chen, Y., Mastalerz, M., Schimmelmann, A., 2014. Heterogeneity of shale documented by micro-FTIR and image analysis. J. Microsc. 256, 177–89. https://doi.org/10.1111/jmi.12169.

Cipolla, C.L., Lolon, E.P., Erdle, J.C., Rubin, B., 2010. Reservoir modeling in shale-gas reservoirs. SPE. Reserv. Eva Eng. 13, 638–653. https://doi. org/10.2118/125530-PA.

Clennell, M.B., Dewhurst, D.N., Brown, K.M., Westbrook, G.K., 1999. Permeability anisotropy of consolidated clays, Geol. Soc. Spec. Publ. 158, 79–96. https://doi.org/10.1144/GSL.SP.1999.158.01.07.

Cui, X., Bustin, A.M.M., Bustin, R.M., 2009. Measurements of gas permeability and diffusivity of tight reservoirs: different approaches and their applications. Geofluids. 9 (3), 208–23. https://doi.org/10.1111/j.1468-8123.2009.00244.x.

Dicker, A.I., Smits, R.M., 1988. A practical approach for determining permeability from laboratory pressure-pulse decay measurements. SPE International Oil and Gas Conference and Exhibition. China. pp. SPE-17578. https://doi. org/10.2118/17578-MS.

Fathi, E., Akkutlu, I.Y., 2009. Matrix heterogeneity effects on gas transport and adsorption in coalbed and shale gas reservoirs. Transport Porous Med. 80, 281–304. https://doi.org/10.1007/s11242-009-9359-4.

Fu, C., Du, Y., Song, W., Sang, S., Pan, Z., Wang, N., 2023. Application of automated mineralogy in petroleum geology and development and CO_2 sequestration: A review. Mar. Pet. Geol. 151, 106206. https://doi.org/ 10.1016/j. marpetgeo.2023.106206.

Gale, J., Holder, J., 2010. Natural fractures in some U.S. shales and their importance for gas production. Geological Society of London, Petroleum Geology Conference. Series 7, 1131–1140. https://doi.org/10.1144/0071131.

Georgi, D., Bespalov, A., Tabarovsky, L., Schoen, J., 2002. On the relationship between resistivity and permeability anisotropy. Society of Petroleum Engineers (SPE), Annual Technical Conference and Exhibition, San Antonio, Texas, USA. Paper 77715. https://doi.org/10.2118/77715-MS.

Ghanizadeh, A., Gasparik, M., Amann-Hildenbrand, A., Gensterblum, Y., Krooss, B.M., 2014a. Experimental study of fluid transport processes in the matrix system of the European organic-rich shales: I. Scandinavian Alum Shale, Mar. Pet. Geol. 51, 79–99. https://doi.org/10.1016/j.marpetgeo.2013.10.013.

Ghanizadeh, A., Amann-Hildenbrand, A., Gasparik, M., Gensterblum, Y., Krooss, B.M., Littke, R., 2014b. Experimental

study of fluid transport processes in the matrix system of the European organic-rich shales: II. Posidonia Shale (Lower Toarcian, northern Germany). Int. J. Coal Geol. 123, 20–33. https://doi.org/10.1016/j.coal.2013.06.009.

Hou, L., Elsworth, D., Zhang, L., Gong, P., Liu, H., 2024. Recalibration of CO_2 storage in shale: prospective and contingent storage resources, and capacity. Energy. 290, 130067. https://doi.org/10.1016/j.energy.2023.130067.

Jacob, H., 1989. Classification, structure, genesis and practical importance of natural solid oil bitumen ("migrabitumen"). Int. J. Coal Geol. 11, 65–9. https://doi.org/10.1016/0166-5162(89)90113-4.

Javadpour, F., 2009. Nanopores and apparent permeability of gas flow in mudrocks (shales and siltstone). J. Can. Pet. Technol. 48 (8), 16–21. https://doi.org/10.2-118/09-08-16-DA.

Jones, S.C., 1997. A technique for faster pulse decay permeability measurements in tight rocks. SPE Format. Eval. 9, 193e199. https://doi.org/10.2118/28450-PA.

Kalantari-Dahaghi, A., 2011. Systematic approach to numerical simulation and modelling of shale gas reservoirs. Int. J. Oil Gas Coal Technol. 4, 209–243. https://doi.org/10.1504/ IJOGCT.2011.040837.

Kanitpanyacharoen, W., Kets, F.B., Wenk, H.-R., Wirth, R., 2012. Preferred Mineral preferred orientation and microstructure in the Posidonia Shale in relation to different degrees of thermal maturity. Clays Clay Miner. 60 (3), 315–329. https://doi.org/10.1346/CCMN.2012.0600308.

Katz, B.J., Arango, I., 2018. Organic porosity: a geochemist's view of the current state of understanding. Org. Geochem. 123, 1–16. https://doi.org/10.1016/j.orggeochem.2018.05.015.

Kwon, O., Kroneberg, A.K., Gangi, A.F., Johnson, B., Herbert, B., 2004. Permeability of illite-bearing shale: anisotropy and effects of clay content and loading. J. Geophys. 109, B10205. https://doi.org/10.1029/2004JB003052.

Leroueil, S., Bouclin, G., Tavenas, F., Bergeron, L., La Rochelle, P., 1990. Permeability anisotropy of natural clays as a function of strain, Can. Geotech. J. 27, 568–579. https://doi.org/10.1139/t90-072.

Li, H., Zhang, B., Chen, X., Miao, F., Chen, L., 2022. Shale Gas Accumulation Conditions Analysis of Cambrian Xiaoyanxi Formation in Anhua Area of Hunan Province. South China Geology. 38 (3), 431-440(in Chinese with English abstract). https://doi.org/ 10.3969/j.issn.2097-0013.2022.03.006.

Li, W., Cao, J., Liang, Y., Masuda, Y., Tsuji, T., Tamura, K., Ishiwata, T., Kuramoto, D., Matsuoka, T., 2024. Evaluation of CO_2 storage and enhanced gas recovery potential in gas shale using kerogen nanopore systems with mesopores and micropores. Chem. Eng. J. 486, 150225. https://doi.org/10.1016/j.cej.2024.150225.

Liu, Q., Sun, M., Sun, X., Liu, B., Ostadhassan, D., Huang, W., Chen, X., Pan, Z., 2023. Pore network characterization of shale reservoirs through state-of-the-art X-ray computed tomography: A review. J. Nat. Gas Sci. Eng. 113, 204967. https://doi.org/10.1016/j.jgsce.2023.204967.

Loucks, R.G., Reed, R.M., Ruppel, S.C., Jarvie, D.M., 2009. Morphology, genesis, and distribution of nanometer-scale pores in siliceous mudstones of the Mississippian Barnett Shale. J. Sediment. Res. 79, 848–861. https://doi.org/ 10.2110/jsr.2009.092.

Loucks, R.G., Reed, R.M., Ruppel, S.C., Hammes, U., 2012. Spectrum of pore types and networks in mudrocks and a descriptive classiffcation for matrix-related mudrock pores. AAPG Bull. 96, 1071–1098. https://doi.org/ 10.1306/ 08171111061.

Luffel, D.L., Hopkins, C.W., Holditch, S.A., Schetter, P.D., 1993. Matrix permeability measurement of gas productive shales. In: Society of Petroleum Engineers (SPE), Annual Technical Conference and Exhibition, Houston, Texas. SPE Paper 26633. https://doi.org/10.2118/26633-MS.

Lyu, C., Yu, H., Jin, J., Xu, W., Huang, H., Zhang, J., Wang, Q., Liu, J., Jiang, W., Liu, H., Wu, H., 2024. Multiphysics phase-field modeling for thermal cracking and permeability evolution in oil shale matrix during in-situ conversion process. Int. J. Rock Mech Min. 176, 105720. https://doi.org/10.1016/ j.ijrmms.2024.105720.

Ma, Y., Zhong, N., Li, D., Pan, Z., Cheng, L., Liu, K, 2015. Organic matter/clay mineral intergranular pores in the Lower Cambrian Lujiaping Shale in the north-eastern part of the upper Yangtze area, China: a possible microscopic mechanism for gas preservation. Int. J. Coal Geol. 137, 38–54. https://doi.org/10.1016/j.coal.2014.11.001.

Ma, Y., Pan, Z., Zhong, N., Connell, L. D., Down, D.I., Lin, W., Zhang, Y., 2016. Experimental study of anisotropic gas

permeability and its relationship with fracture structure of Longmaxi shales, Sichuan basin, China. Fuel 180, 106-115. https://doi.org/10.1016/j.fuel.2016.04.029.

Ma, Y., Ardakani, O.H., Zhong, N., Liu, H., Huang, H., Larter, S., Zhang, C., 2020. Possible pore structure deformation effects on the shale gas enrichment: An example from the Lower Cambrian shales of the Eastern Upper Yangtze Platform, South China. Int. J. Coal Geol. 217, 103349. https://doi.org/10.1306/07231212048.

Ma, Y. S., Guo, X., Guo, T., Huang, R., Cai, X., Li, G., 2007. The Puguang gas field: New giant discovery in the mature Sichuan Basin, southwest China. AAPG Bull. 91, 627–643. https://doi.org/10.1306/11030606062.

Mastalerz, M., Drobniak, A., Stankiewicz, A.B., 2018. Origin, properties, and implications of solid bitumen in source-rock reservoirs: A review. Int. J. Coal Geol. 95, 14–36. https://doi.org/10.1016/j.coal.2018.05.013.

Meng, Q., Wang, E., Hu, J., 2005. Mesozoic sedimentary evolution of the northwest Sichuan basin: implication for continued clockwise rotation of the South China block. GSA Bull. 117, 396–410. https://doi.org/10.1130/B25407.1.

Metwally, Y.M, Sondergeld, C.H., 2011. Measuring low permeabilities of gas-sands and shales using a pressure transmission technique. Int. J. Rock Mech Min Sci. 48, 1135–44. https://doi.org/10.1016/j.ijrmms.2011.08.004.

Milliken, K.L., Rudnicki, M., Awwiller, D.N., Zhang, T., 2013. Organic matter-hosted pore system, Marcellus Formation (Devonian), Pennsylvania. AAPG Bull. 97, 177–200. https://doi.org/10.1306/07231212048.

Mukherjee, M., Vishal, V., 2023. Gas transport in shale: a critical review of experimental studies on shale permeability at a mesoscopic scale. Earth Sci. Rev. 104522. https://doi.org/10.1016/j.earscirev.2023.104522.

Ougier-Simonin, A., Renard, F., Boehm, C., Vidal-Gilbert, S., 2016. Microfracturing and microporosity in shales. Earth Sci. Rev. 162, 198-226. https://doi.org/10.1016/j.earscirev.2016.09.006.

Pan, Z., Ma, Y., Connell, L.D., Down, D.I., Camilleri, M., 2015. Measuring anisotropic permeability using a cubic shale sample in a triaxial cell. J. Nat. Gas Sci. Eng. 26, 336–44. https://doi.org/10.1016/j.jngse.2015.05.036.

Pathi, V.S.M., 2008. Factors affecting the permeability of gas shales. Master's thesis, University of British Columbia, Vancouver, Canada. p 189. https://doi.org/10.14288/1.0052381.

Patzek, T.W., Male, F., Marder, M., 2013. Gas production in the Barnett Shale obeys a simple scaling theory. Proc. Natl. Acad. Sci. 110 (49), 19731–19736. https://doi.org/10.1073/ pnas.1313380110.

Peng, S., Marone, F., Dultz, S., 2014. Resolution effect in X-ray microcomputed tomography imaging and small pore's contribution to permeability for a Berea sandstone. J. Hydrol. 510, 403–411. https://doi.org/10.1016/j.jhydrol. 2013.12.028.

Sasaki, T., Rutqvist, J., 2024. Effects of anisotropic shale creep on the stress and permeability evolution of a geological nuclear waste repository. Tunn. Undergr. Sp Technol. 144, 105537. https://doi.org/10.1016/j.tust.2023.105537.

Schmitt, M., Fernandes, C.P., Wolf, F. G., da Cunha Neto, J.A.B., Rahner, C.P., dos Santos, V.S.S., 2015. Characterization of Brazilian tight gas sandstones relating permeability and Angstrom-to micron-scale pore structures. J. Nat. Gas Sci. Eng. 27, 785-807. https://doi.org/10.1016/j.jngse.2015.09.027.

Shi, R., Liu, J., Wang, X., Wei, M., Elsworth, D., 2021. A critical analysis of shale laboratory permeability evolution data. Energy. 236, 121405. https://doi.org/10.1016/j.energy.2021.121405.

Sun, M., Yu, B., Chen, S., Xia, W., Ye, R., 2015. Reservoir characteristics and adsorption capacity of the lower Cambrian niutitang formation shale in southeaster of Chongqing: a case study of well Yuke 1 and well Youke 1. J. Northeast Petrol. Univ. 39, 69–79 (in Chinese with English abstract).

Wenk, H.-R., Voltolini, M., Mazurek, M., Loon, V.L., 2008. Preferred orientations and anisotropy in shales: Callovo-Oxfordian shale (France) and Opalinus Clay (Switzerland). Clays clay miner. 56 (3), 285-306. https://doi.org/ 10.1346/CCMN.2008.0560301.

Yang, Y., Aplin, A.C., 1998. Influence of lithology and compaction on the pore size distribution and modelled permeability of some mudstones from the Norwegian margin. Mar. Pet. Geol. 15, 163–175. https://doi.org/ 10.1016/S0264-8172(98)00008-7.

Yang, Y., Aplin, A., 2007. Permeability and petrophysical properties of 30 natural mudstones, J. Geophys. Res. 112,

B03206. https://doi.org/10.1029/2005JB004243.

Zeng, W., Zhang, J., Ding, W., Zhao, S., Zhang, Y., Liu, Z., Jiu, K., 2013. Fracture development in Paleozoic shale of Chongqing area (South China). Part one: Fracture characteristics and comparative analysis of main controlling factors. J. Asia Earth Sci. 75, 251–266. https://doi.org/10.1016/j.jseaes.2013.07.014.

Zhang, G., Zhang, B., Yuan, X., Xiao, Q., 2001. Qinling Orogenic Belt and Continental Dynamics. Science Press, Beijing, China, pp. 117–321 (in Chinese with English abstract).

Zhao, W., Li, J., Yang, T., Wang, S., Huang, J., 2016. Geological difference and its significance of marine shale gases in South China. Petrol Explor Develop. 43 (4), 547-559. https://doi.org/10.1016/S18763804(16)30065-9.

Zhao, J., Sun, M., Pan, Z., Liu, B., Ostadhassan, M., Hu, Q., 2022. Effects of pore connectivity and water saturation on matrix permeability of deep gas shale. Adv. Geo-Energy Res. 6 (1), 54-68. https://doi.org/10.46690/ager.2022.01.05.

Zhu, H., Ju, Y., Huang, C., Qi, Y., Ju, L., Yu, K., Li, W., Feng, H., Qiao, P., 2019. Petrophysical properties of the major marine shales in the Upper Yangtze Block, south China: a function of structural deformation. Mar. Petrol. Geol. 110, 768–786. https://doi.org/10.1016/j.marpetgeo.2019.08.003.

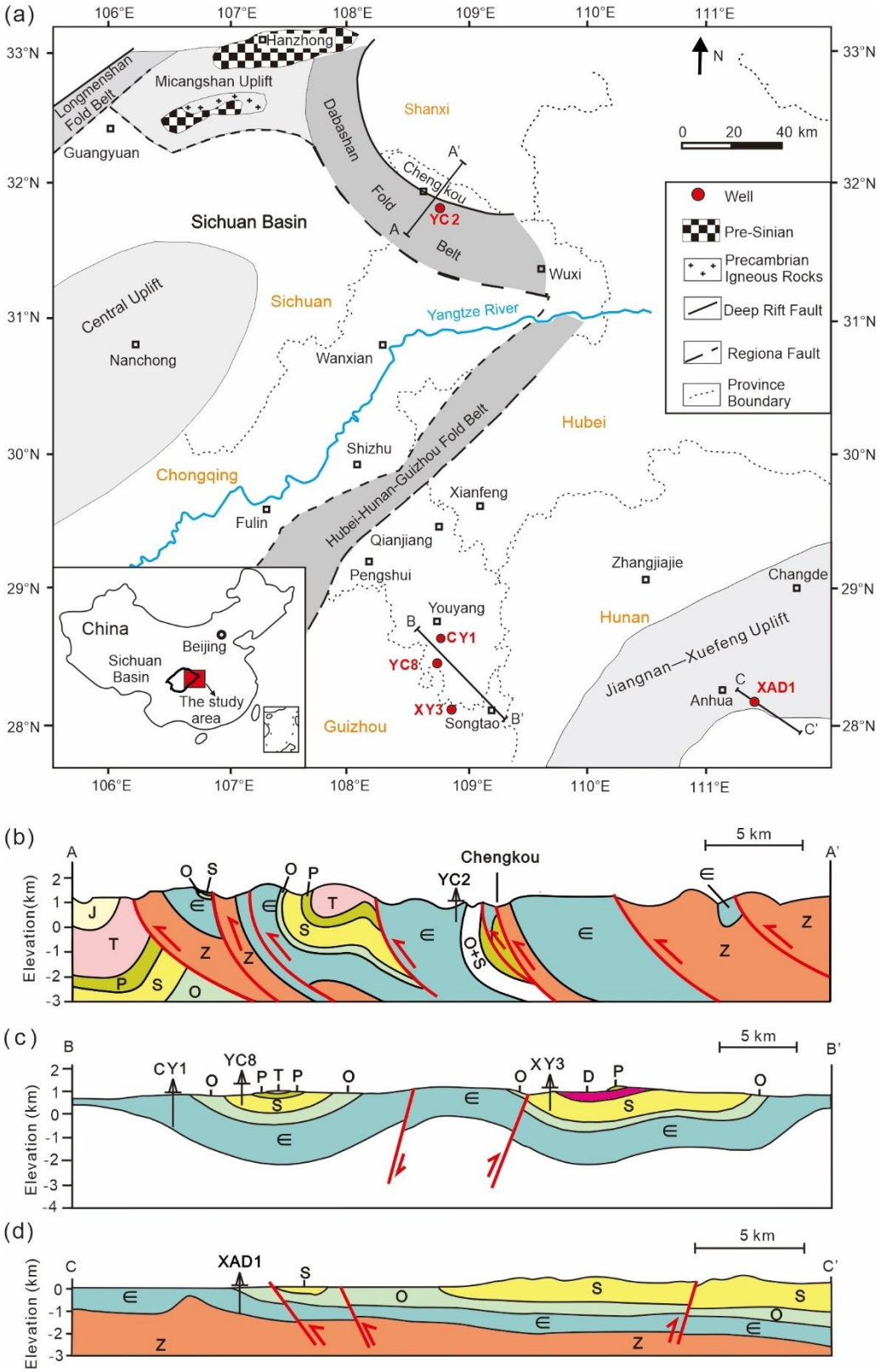

Fig.1. Location of shale gas wells in the upper Yangtze Platform superimposed on the (a) Regional tectonic sketch-map (after Ma et al., 2007); (b), (b) and (d) Simplified geological cross-section for AA' (after Ma et al., 2020), BB' (after Ma et al., 2020), and CC'(after Li et al., 2022). See (a) for the location of the cross-section.

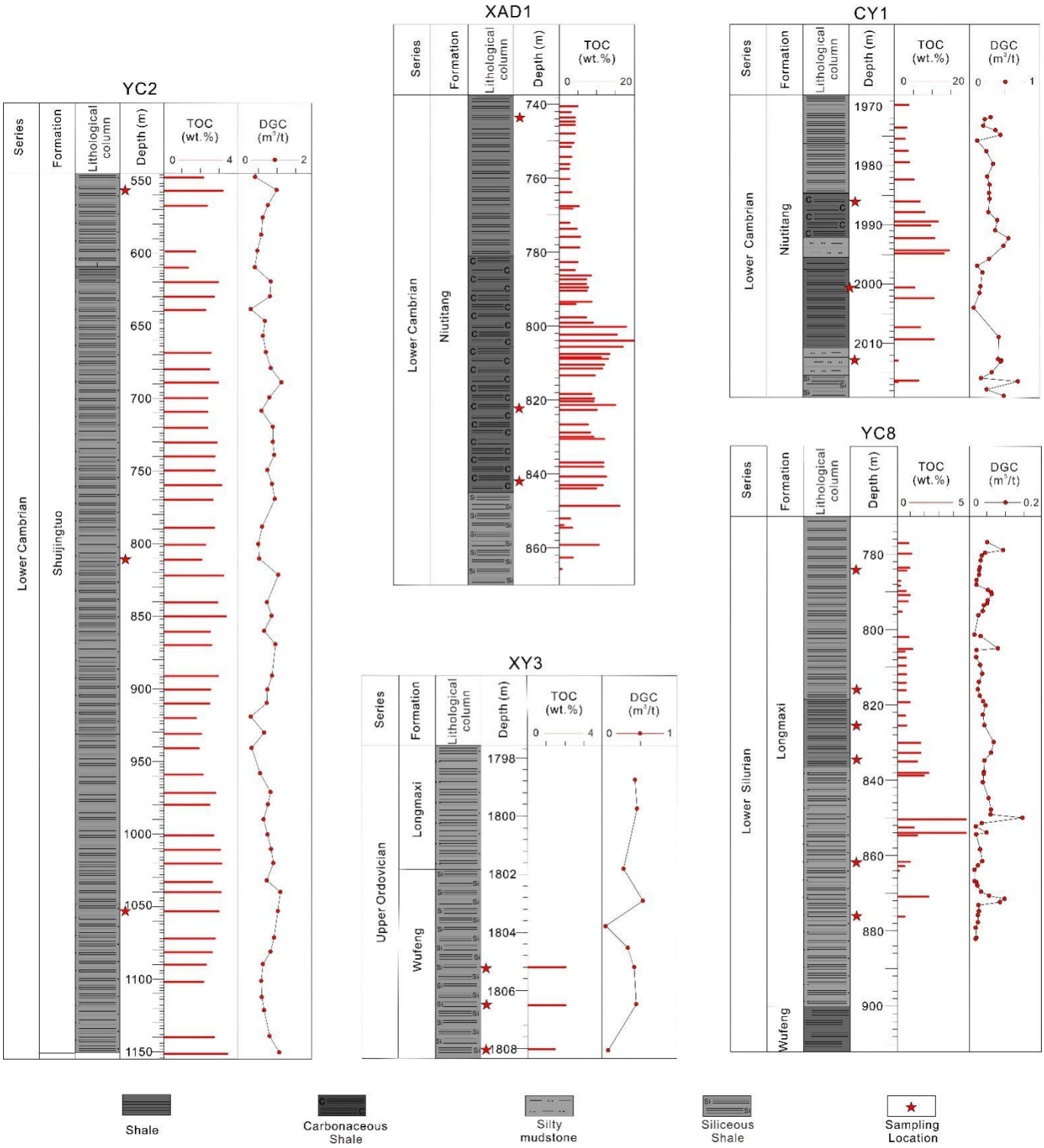

Fig.2. Integrated columns showing the lithology, TOC content and desorbed gas content (DGC) in the study area. See **Fig.1** for the location of the wells.

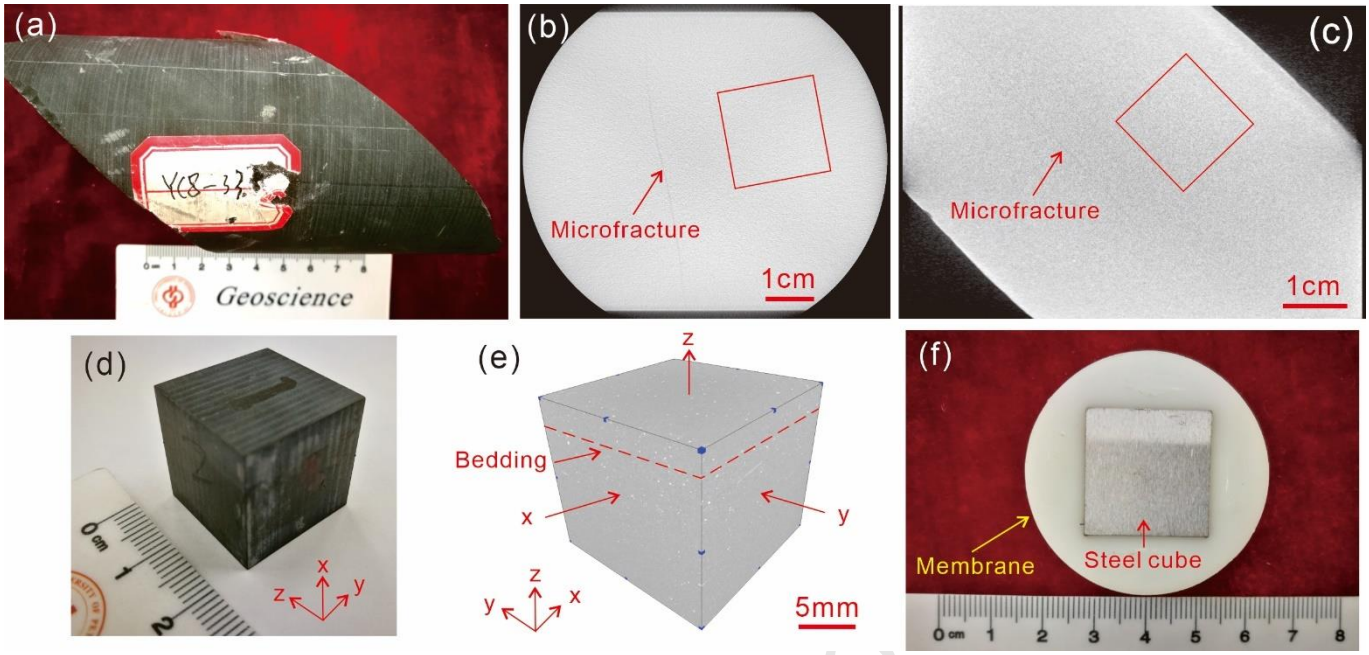

Fig.3. Schematic diagram shows the workflow of cubic sample preparation for matrix permeability measurement in three directions. (a) Shale core sample, YC8-33; (b) and (c) X-ray CT slice shows the cross and vertical section of shale core sample in (a), respectively. The red box mark the frame for cubic shale preparation; (d) Cubic shale sample; (e) 3D reconstruction of cubic shale by X-ray CT images in (d); (f) 3D-printed polymer membrane with a steel test cube installed.

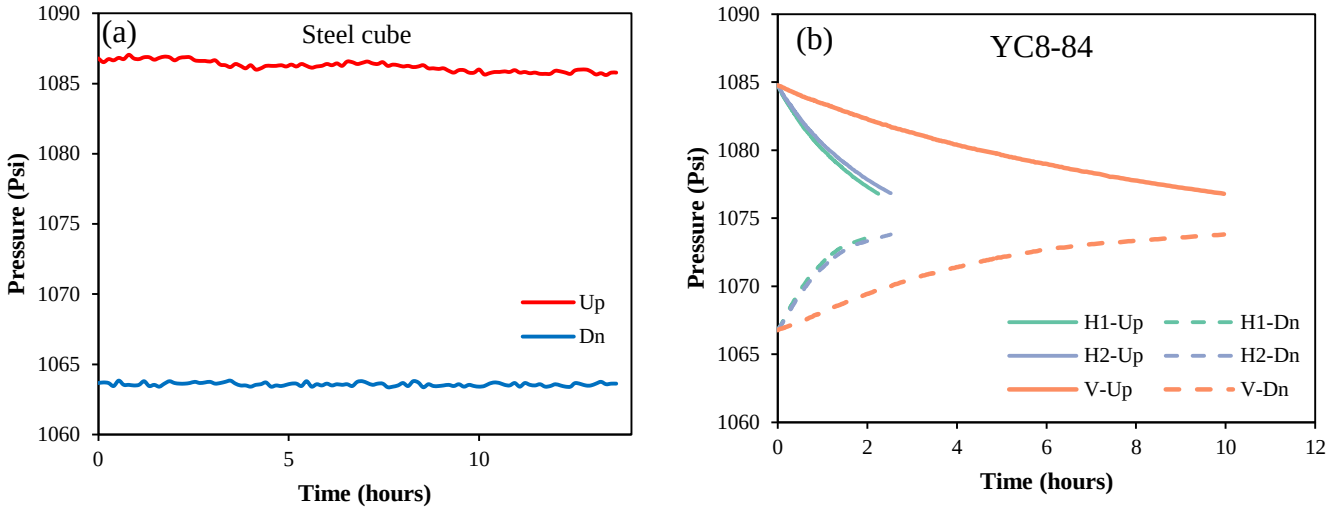

Fig.4. Pressure recordings in upstream and downstream compartments of the permeameter for a steel test cube (a) and a cubic shale sample in two horizontal and one vertical direction placed inside the 3D-printed polymer membrane (b). Up-Upstream; Dn-Downstream.

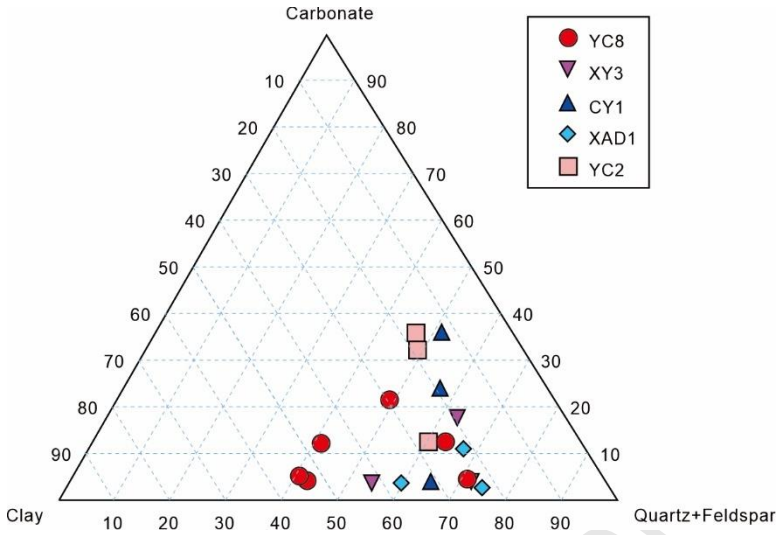

Fig.5. Mineralogical ternary plot of the shale samples in the five studied wells.

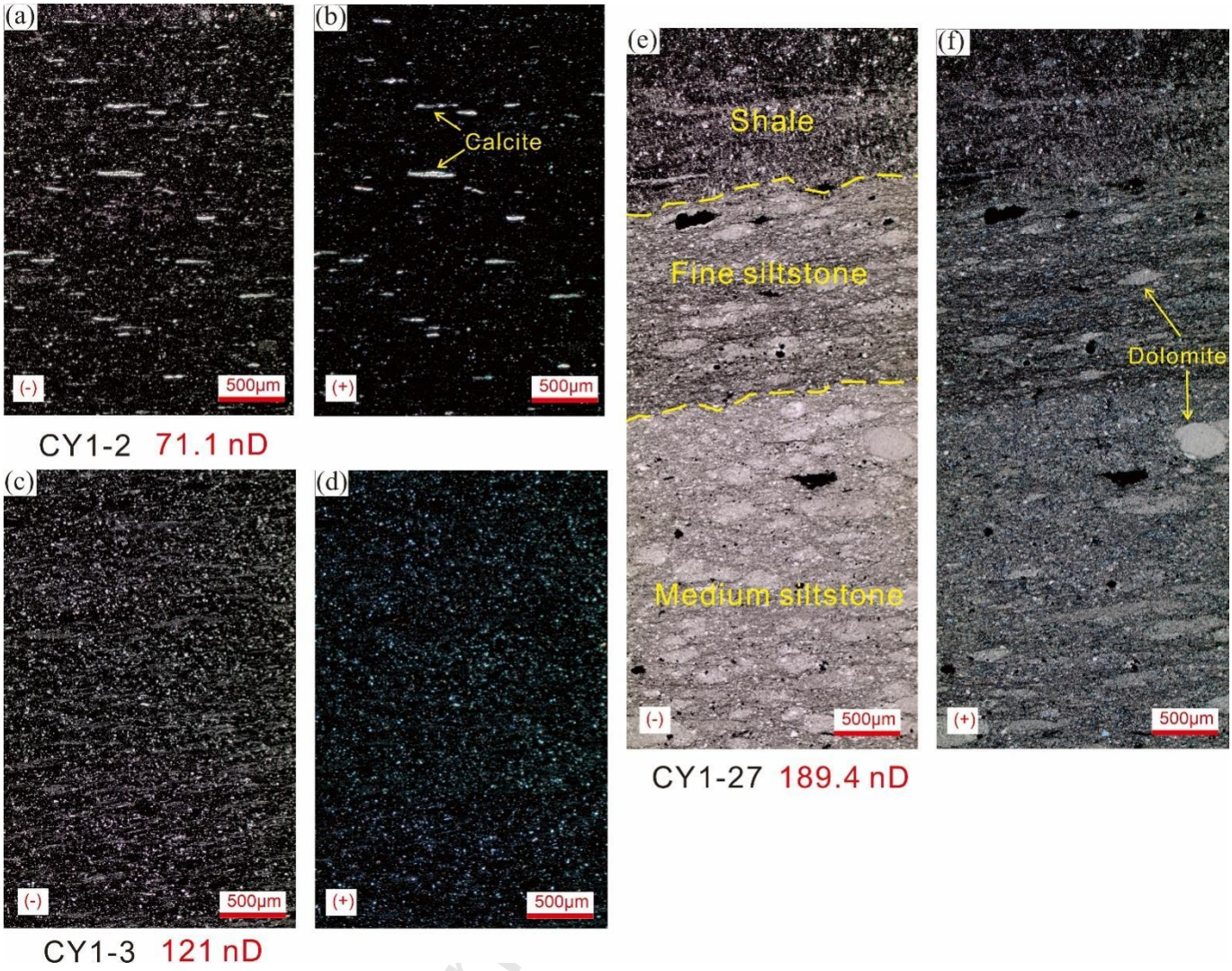

Fig.6. Transmitted light thin section images for three Lower Cambrian shale samples in SE Chongqing with different matrix permeability. (a) and (b), fine laminated siliceous and calcite cement with clay minerals, CY1-2; (c) and (d), thin evenly parallel laminated shale, CY1-3; (e)and (f), a transition from medium siltstone to shale, CY1-27.
(-) plane-polarized light; (+) cross polarized light.

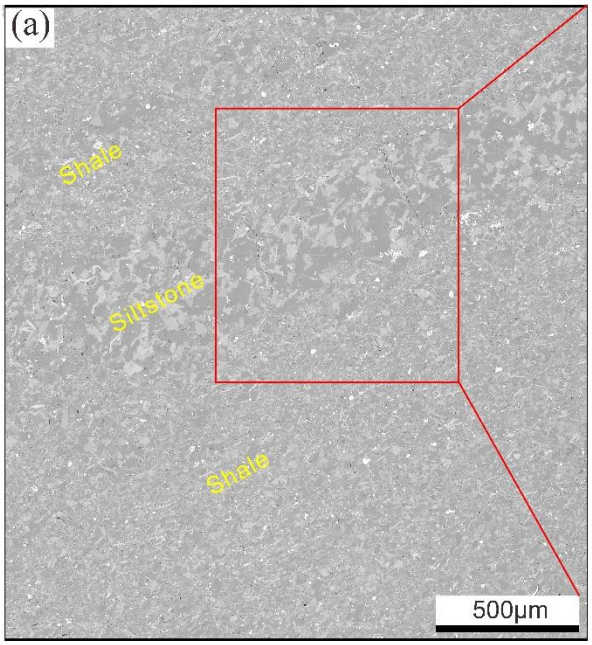

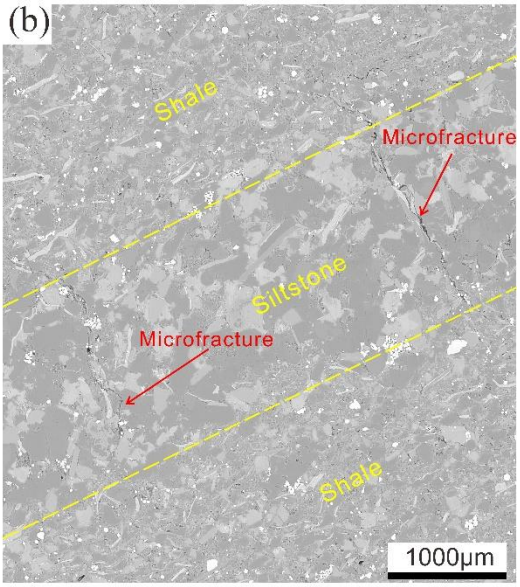

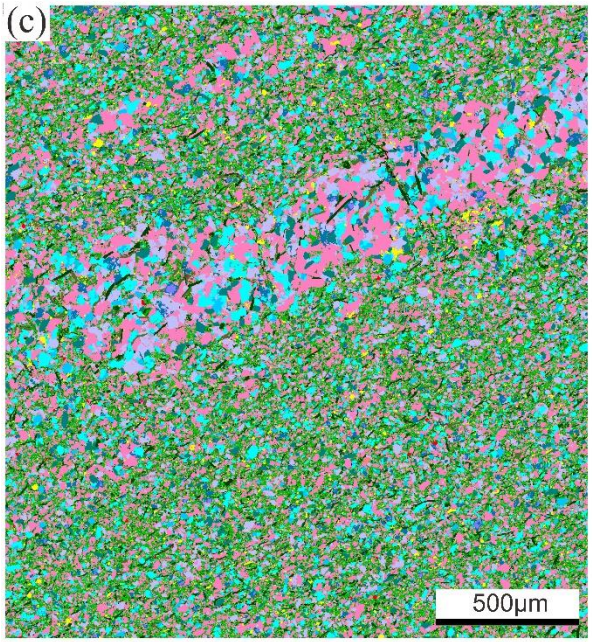

Quartz
Illite
Calcite
Chlorite
Muscovite
Oligoclase
Pyrite
Ankerite
Albite
Orthoclase
Dolomite
Rutile
Apatite
Zircon
Organic
Unknown

Mineral	Wt%	Area%
Quartz	32	33.44
Illite	24.7	24.59
Calcite	8.88	8.97
Chlorite	3.59	3.1
Muscovite	6.5	6.31
Oligoclase	3.57	3.69
Pyrite	3.61	1.97
Ankerite	2.37	2.13
Albite	8.66	9.04
Orthoclase	3.76	4.03
Dolomite	0.26	0.25
Rutile	0.38	0.25
Apatite	0.27	0.23
Zircon	0.03	0.02
Organic	0.06	0.14
Unknown	1.36	1.84

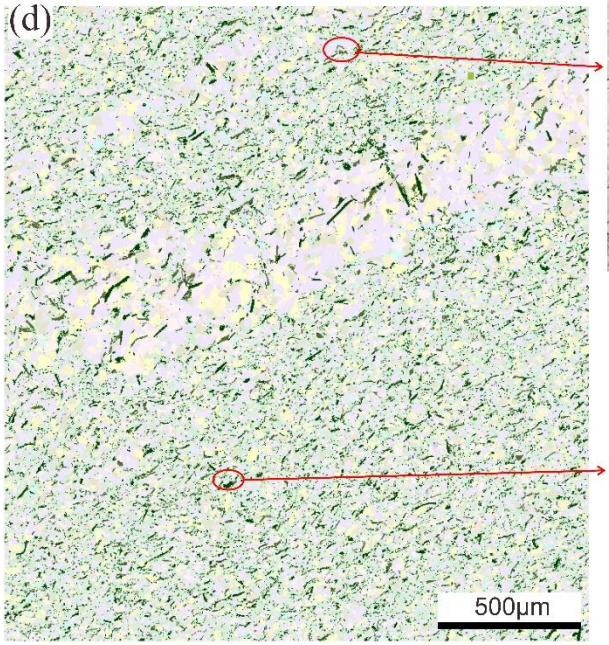

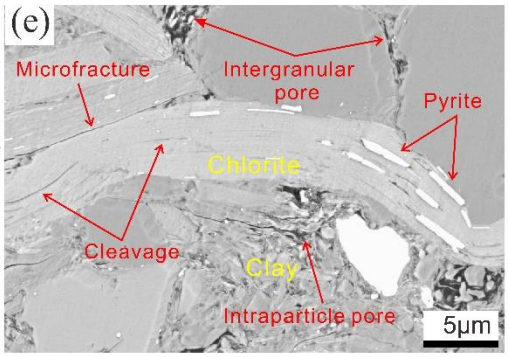

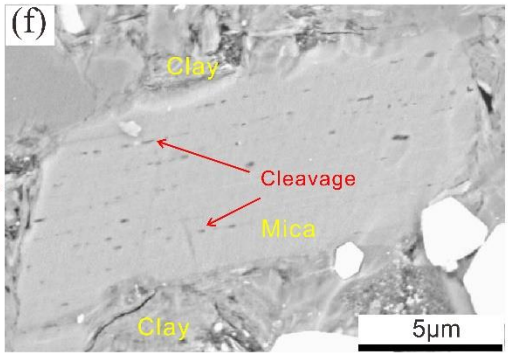

Fig.7. SEM and QEMSCAN images showing the lamination, microfractures and pores associated with minerals, YC8-54. (a) Backscattered electron (BSE) image showing the bedding between shale and siltstone; (b) Close-up view of the lamination shown in (a). High angle microfractures developed in the siltstone and pinch out in the shale; (c) QEMSCAN image corresponding to the BSE image (a) with the mineral composition; (d) Distribution of mica and chlorite extracted from (c) showing its preferred orientation parallel to bedding; (e) Amplified view of the chlorite in (d) showing the cleavage and pore-filling pyrite; (f) Amplified view of the mica in (d) showing the cleavage.

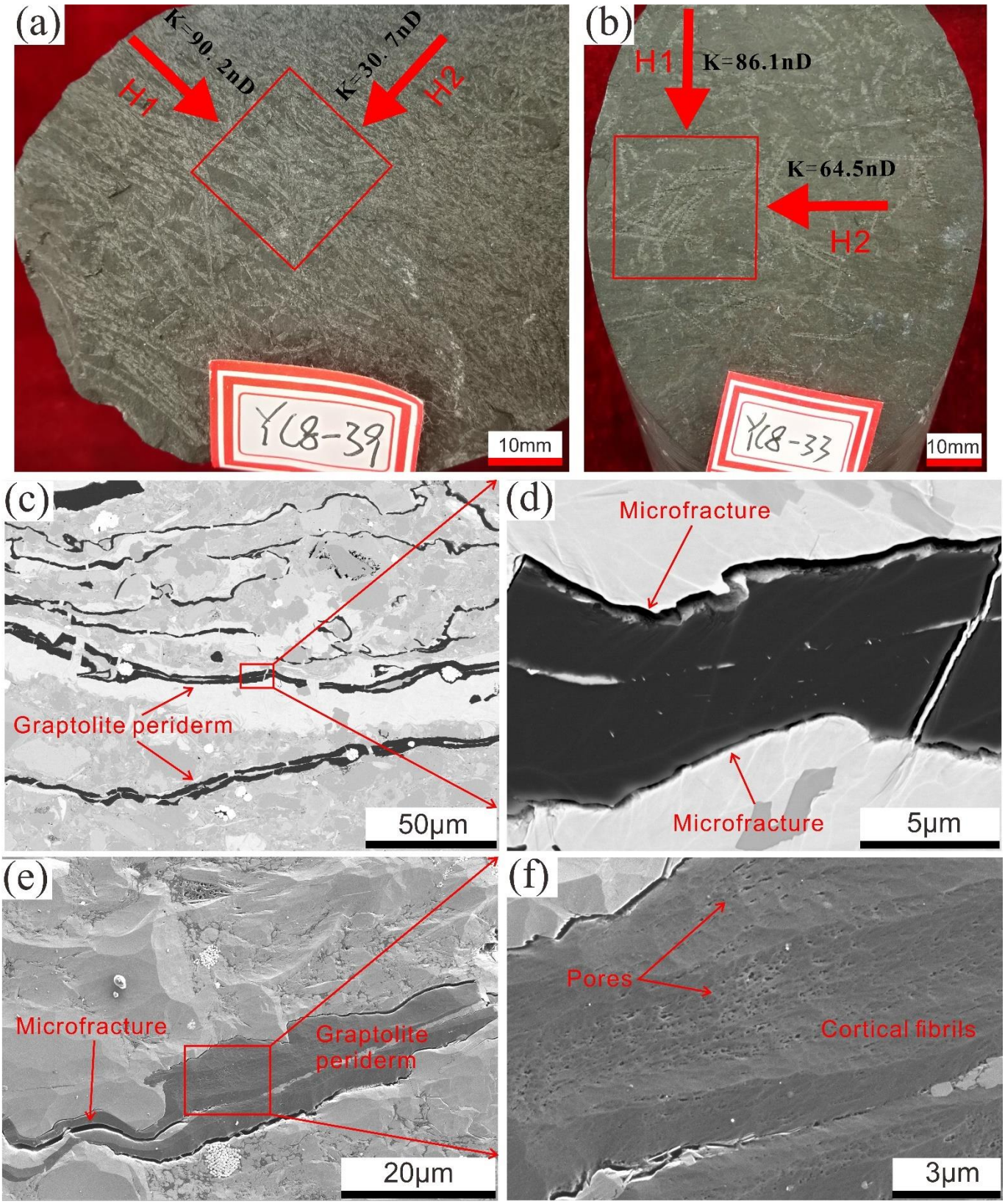

Fig.8. Photographs showing the Lower Silurian Longmaxi shales developing graptolites with directional and random arrangements and BSE images showing the pore structure of graptolite. (a) Photo of the core shale sample showing graptolites with preferred orientation, YC8-39; (b) Photo of the core shale sample with graptolites arranged randomly, YC8-33. (c) BSE image showing the graptolite periderms in a section perpendicular to bedding, YC8-39; (d) Part of the graptolite periderm in (c) to show the microfractures

between graptolite and minerals; (e) BSE image showing the microfractures between graptolite and minerals in a section perpendicular to bedding, YC8-39; (f) Enlarged view of graptolite periderm showing the nanometer-sized spindle-shaped pores between cortical fibrils in a cortical bandage.

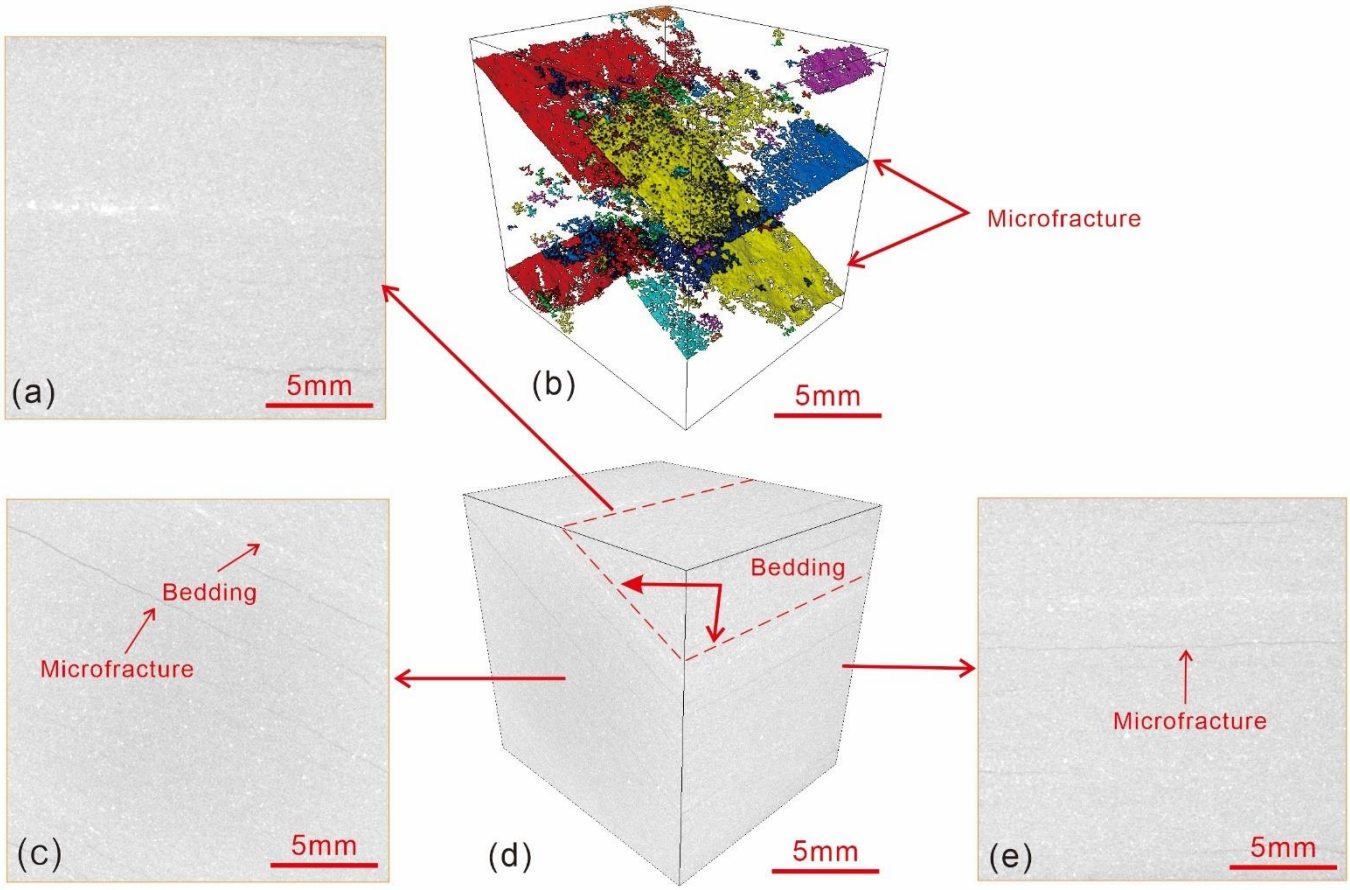

Fig.9. X-ray CT results showing the microfracture in the Shuijing shale in NE Chongqing, YC2-17. Cubic shale is cut in the vertical direction of the formation. (a) (c) (e) CT slice of cubic shale in (d) showing one vertical and two horizontal directions against with formation; (b) Delineated microfractures of the 3D block from (d); (d) 3D reconstruction of the cubic shale from gray-scale images.

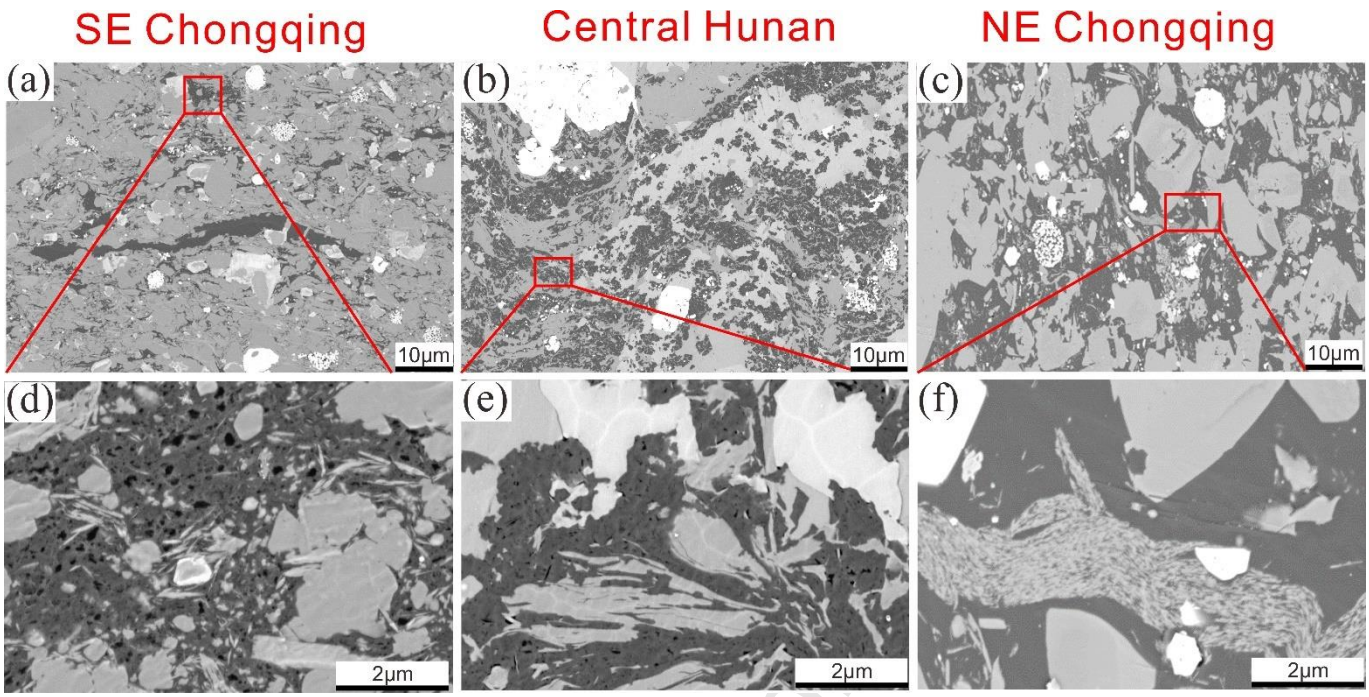

Fig.10. BSE images of the Lower Cambrian shales from three different tectonic deformation zones showing the OM pore structure with a consistent scale bar. (a) Pores are rounded or elliptic within the solid bitumen in SE Chongqing, CY1-2,; (b) Small elongated pores or pinhole pores within the solid bitumen in Central Hunan, XAD1-2; (c) No visible pores within the solid bitumen in NE Chongqing, YC2-65.

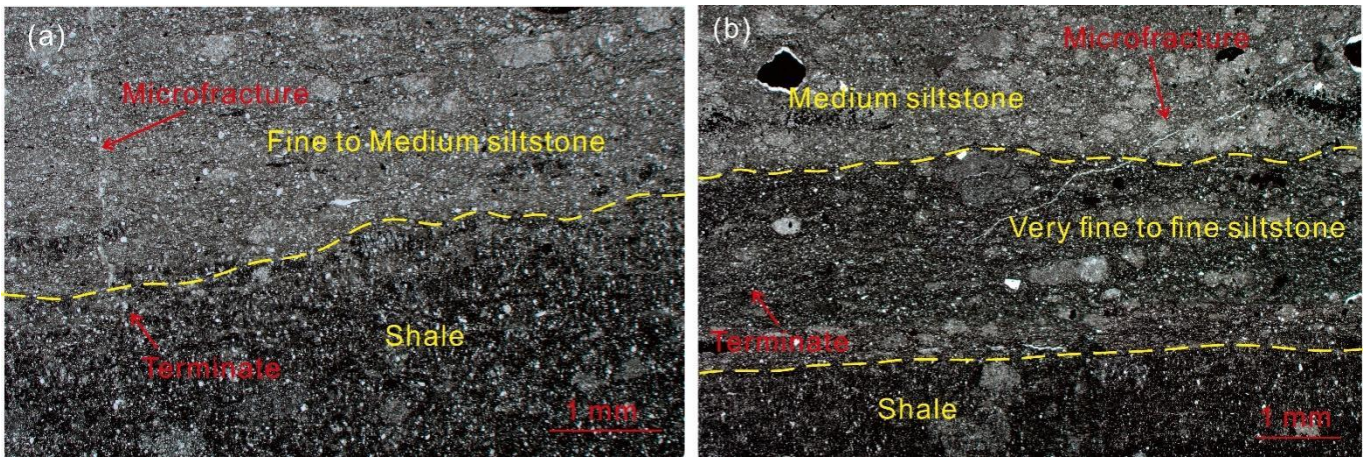

Fig.11. Transmitted light thin images perpendicular to bedding showing that microfractures in siltstone and terminate at shale, CY1-27. (a) in x-direction; (b) in y-direction.

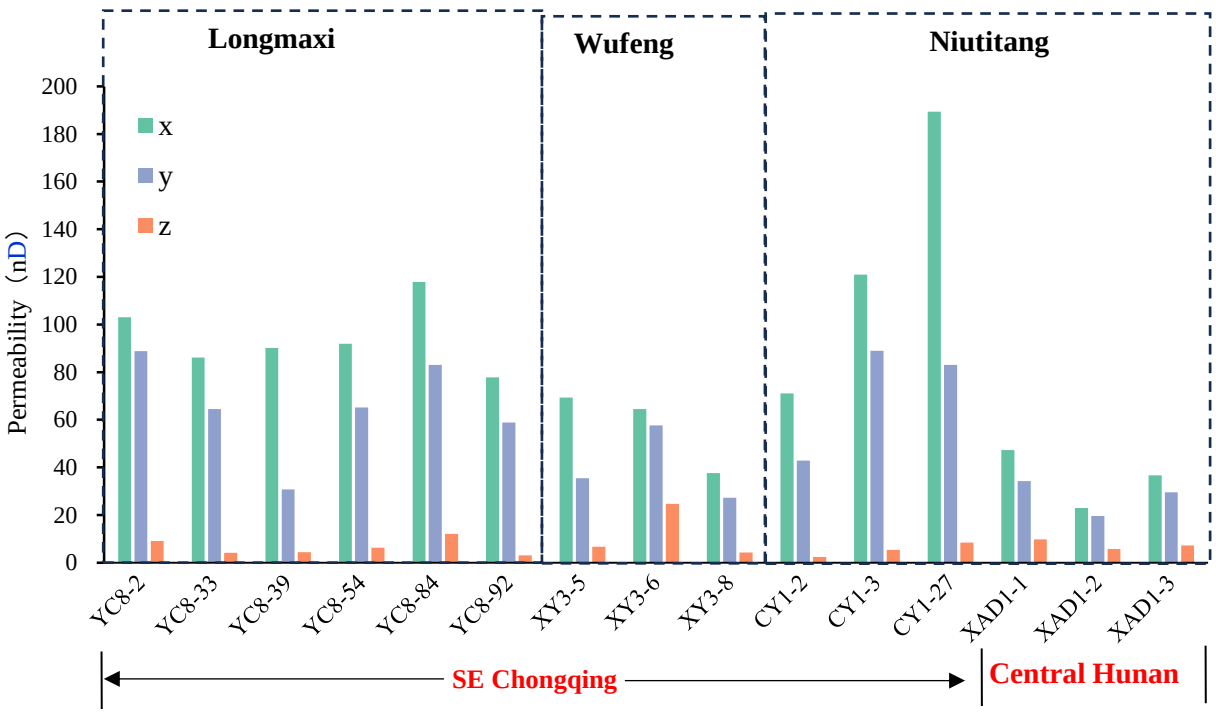

Fig.12. Measured matrix permeability in three directions of the Niutitang, Wufeng and Longmaxi shales in southeast Chongqing and Central Hunan.

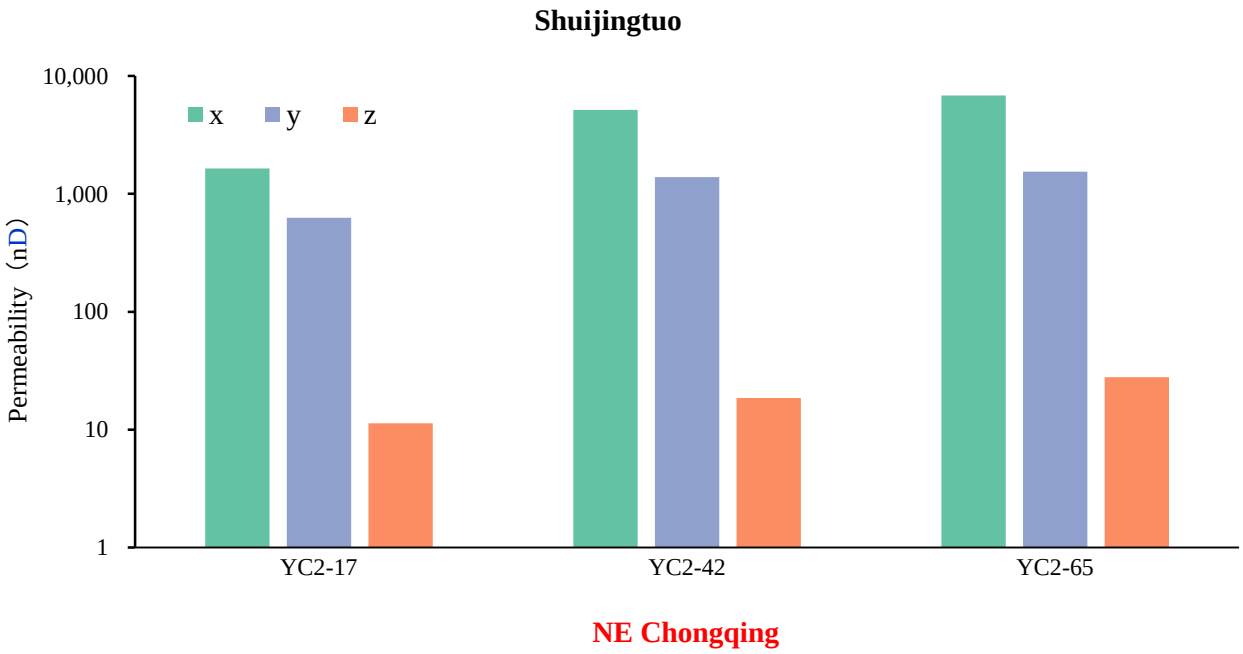

Fig.13. Measured permeability in three directions of the Shuijingtuo shales in northeast Chongqing.

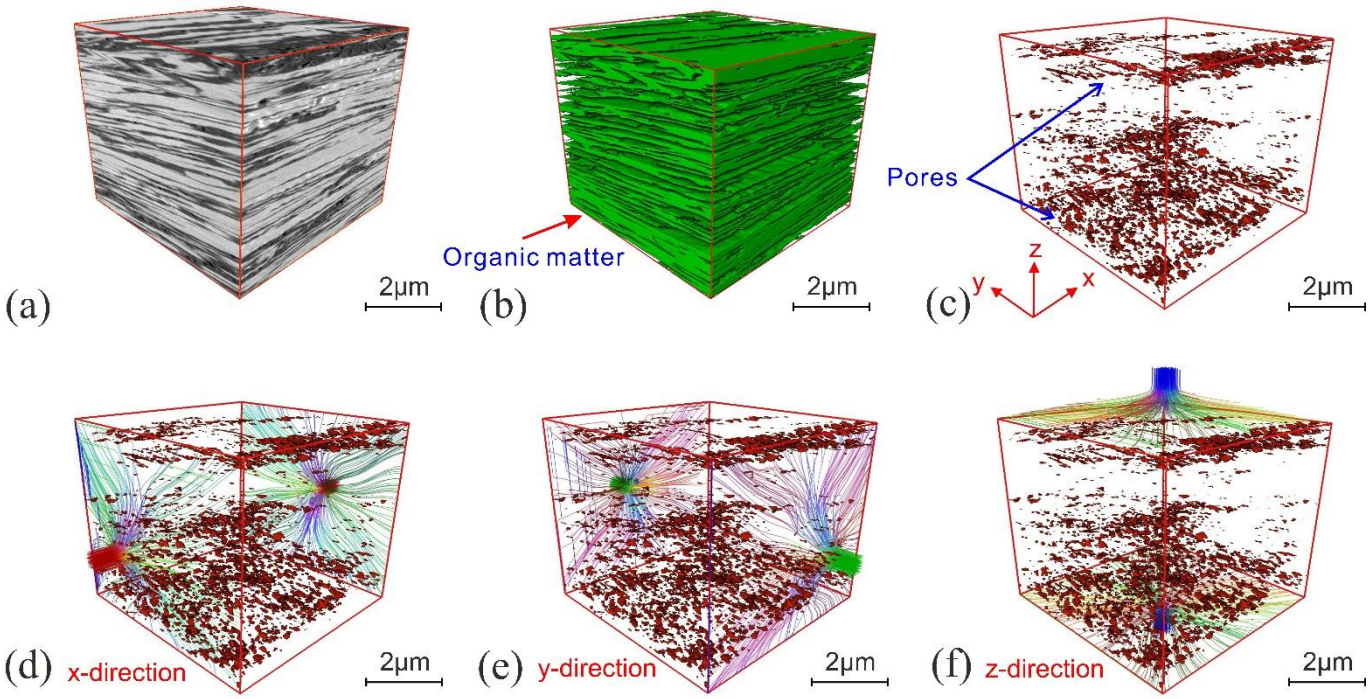

Fig.14. 3D reconstruction of a mica volume from FIB-SEM images and permeability simulation of the pore network of the mica in three directions, XAD1-2-A. (a) 3D solid block rendered from BSE images; (b) Delineated organic matter of the 3D block from (a); (c) Delineated pores of the 3D block from (a); (g) (h) (f) showing simulation of permeability of pore network in (f) in x, y and z directions, respectively. Visualization of the illuminated streamlines representing the fluid velocity field in the permeability simulation.

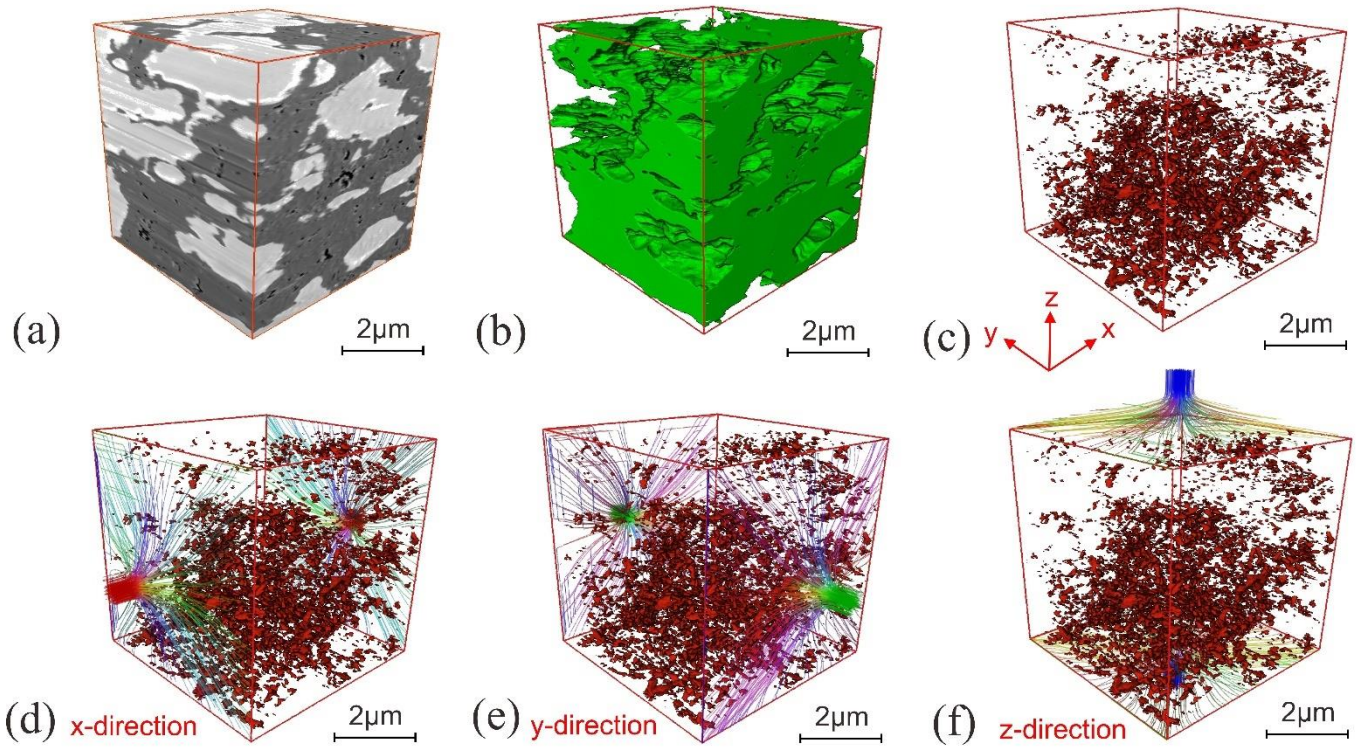

Fig.15. 3D reconstruction of a shale volume from FIB-SEM images and permeability simulation of the pore network of the solid bitumen in three directions, XAD1-2-B. (a) 3D solid block rendered from BSE images; (b) Delineated organic matter of the 3D block from (a); (c) Delineated pores of the 3D block from (a); (g) (h) (f) showing simulation of permeability of pore network in (f) in x, y and z directions, respectively.

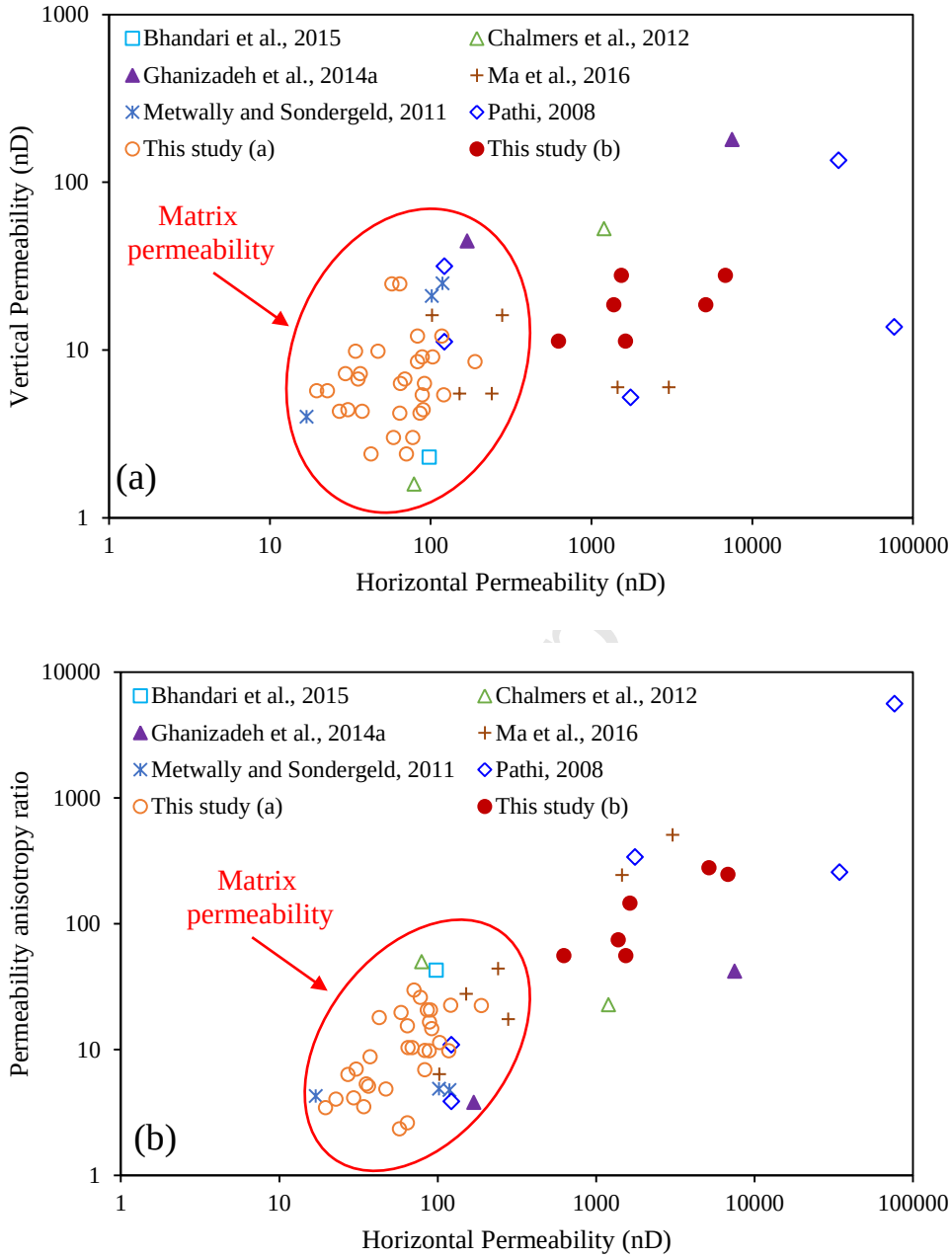

Fig.16. Plots showing horizontal permeability versus vertical permeability (a) and permeability anisotropy ratio of shales in this study and in literature.
This study (a): measured matrix permeability of the 15 shales in this study;
This study (b): measured permeability of 3 Lower Cambrian shales in NE Chongqing developed with microfractures in this study.

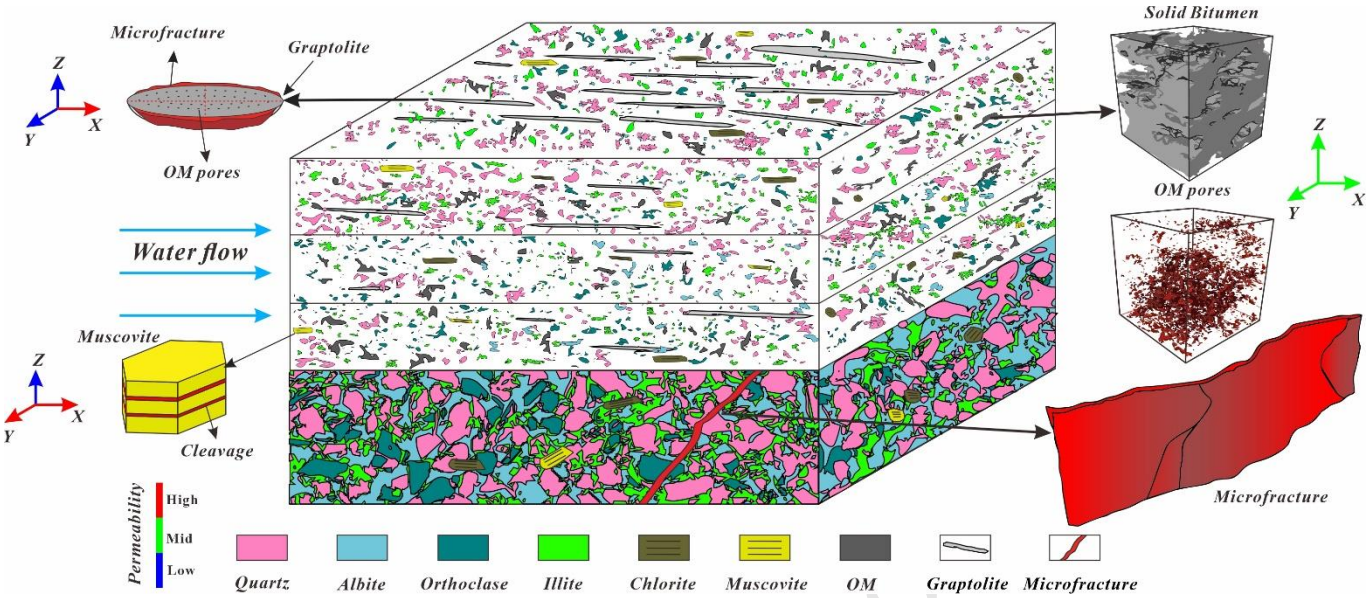

Fig.17. Schematic diagram showing the geological control on shale matrix permeability

Table 1. List of studied samples with basic geological information and analytical results of TOC content, equivalent vitrinite reflectance ($EqVR_o$), desorbed gas content (DGC), N_2 and CO_2 adsorption analysis.

Region	Sample ID	Well	Series	Formation	Depth (m)	TOC (%)	$EqVR_o$ (%)	DGC (m^3/t)	Meso- to Macropore surface area N_2 (m^2/g)	Meso- to Macropore volume-N_2 (cm^3/g)	Micropore surface area-CO_2 (m^2/g)	Micropore volume-CO_2 (cm^3/g)
SE CQ (Southeast Chongqing)	YC8-2	YC8	Lower Silurian	Longmaxi	784.13	0.62	2.3	0.03	11.00	0.013	8.80	0.003
	YC8-33				815.93	0.63	2.31	0.02	12.14	0.02	9.02	0.003
	YC8-39				825.43	0.64	2.26	0.04	10.97	0.01	7.98	0.003
	YC8-54				834.83	1.32	2.26	0.04	9.89	0.009	7.37	0.002
	YC8-84				861.53	0.86	2.36	0.03	7.71	0.011	3.68	0.001
	YC8-92				875.82	0.59	2.22	0.02	4.98	0.006	2.90	0.001
	XY3-5	XY3	Upper Ordovician	Wufeng	1805.24	2.05	2.32	0.51	2.08	0.003	0.66	0
	XY3-6				1806.54	2.01	2.24	0.56	6.97	0.01	4.06	0.001
	XY3-8				1808.04	1.65	2.36	0.16	6.47	0.007	4.51	0.001
	CY1-2	CY1	Lower Cambrian	Niutitang	1986.45	7.61	3.09	0.27	23.55	0.015	25.09	0.007
	CY1-3				2000.48	5.40	3.03	0.15	24.35	0.01	29.43	0.008
	CY1-27				2012.95	0.72		0.42	4.66	0.004	4.62	0.001
Central Hunan	XAD1-1	XAD1	Lower Cambrian	Niutitang	743.30	4.21	2.97		9.13	0.006	11.10	0.003

	XAD1-2				822.10	10.08	3.23		5.02	0.007	14.92	0.006
	XAD1-3				841.90	12.55			6.41	0.005	15.34	0.006
NE CQ (Northeast Chongqing)	YC2-17	YC2	Lower Cambrian	Shuijingtuo	556.75	3.11	2.63	1.06	7.33	0.005	11.44	0.003
	YC2-42				810.40	2.05		0.59	6.96	0.004	7.39	0.002
	YC2-65				1050.20	3.05		0.79	5.45	0.005	9.62	0.003

Table 2. Mineral composition of the studied samples.

Sample ID	Mineral composition（wt.%）						
	Quartz	K-feldspar	Plagioclase	Calcite	Dolomite	Pyrite	Total clay
YC8-2	34.3	0.2	5.0	1.2	4.2	2.2	52.9
YC8-33	34.5	1.2	5.6	3.8	0.5	2.1	52.3
YC8-39	32.3	1.1	6.7	5.3	7.0	1.7	45.7
YC8-54	36.3	1.9	8.1	15.1	5.9	4.6	28.1
YC8-84	44.8	7.0	17.7	4.5	0.4	1.7	24.1
YC8-92	43.0	5.7	12.6	9.5	3.2	2.2	23.8
XY3-5	48.4	2.8	8.6	8.7	8.4	4.4	18.7
XY3-6	56.5	2.1	10.0	0.0	4.0	4.3	23.0
XY3-8	40.6	3.9	9.5	1.5	2.4	0.0	42.1
CY1-2	45.9	3.4	8.9	3.9	0.0	9.6	28.2
CY1-3	38.6	4.5	6.8	10.3	11.1	11.5	17.1
CY1-27	44.9	0.7	4.3	0.3	35.0	2.5	12.3
XAD1-1	49.2	1.2	4.2	3.6	0.0	8.1	33.7
XAD1-2	68.4	2.1	0.0	2.7	0.0	5.1	21.7
XAD1-3	58.6	4.4	0.0	3.3	7.1	6.2	20.4
YC2-17	37.2	1.3	19.2	6.1	6.5	3.2	26.4
YC2-42	30.5	0.5	14.0	17.6	17.6	2.9	16.8
YC2-65	33.0	0.5	13.4	18.4	13.2	2.7	18.5

Table 3. Anisotropic matrix permeability and porosity of shale samples in this study.

Region	Sample ID	Depth(m)	Formation	Direction	Permeability (nD)	K_x/k_y [a]	$K_{Horizontal}/k_{Vertical}$ [b]	Porosity（%）
SE Chongqing	YC8-2	784.13	Longmaxi	x	103.1	1.2	11.3	1.10
				y	88.8		9.8	
				z	9.1			
	YC8-33	815.93		x	86.1	1.3	20.5	0.49
				y	64.5		15.4	0.50
				z	4.2			
	YC8-39	825.43		x	90.2	2.9	20.5	0.87
				y	30.7		7.0	
				z	4.4			
	YC8-54	834.83		x	91.9	1.4	14.6	0.45
				y	65.2		10.3	
				z	6.3			
	YC8-84	861.53		x	117.9	1.4	9.7	1.20
				y	83.1		6.9	1.21
				z	12.1			
	YC8-92	875.82		x	77.8	1.3	25.9	0.26
				y	58.9		19.6	
				z	3			
	XY3-5	1805.24	Wufeng	x	69.3	2.0	10.3	1.14
				y	35.5		5.3	
				z	6.7			
	XY3-6	1806.54		x	64.5	1.1	2.6	1.02
				y	57.6		2.3	1.04
				z	24.7			
	XY3-8	1808.04		x	37.6	1.4	8.7	0.69
				y	27.2		6.3	
				z	4.3			
	CY1-2	1986.45	Niutitang	x	71.1	1.7	29.6	0.49

				y	42.8		17.8	
				z	2.4			
	CY1-3	2000.48		x	121	1.4	22.4	0.59
				y	89		16.5	0.61
				z	5.4			
	CY1-27	2012.95		x	189.4	2.3	22.3	0.74
				y	83.1		9.8	
				z	8.5			
	XAD1-1	743.3		x	47.3	1.4	4.8	0.63
				y	34.3		3.5	
				z	9.8			
	XAD1-2	822.1		x	22.9	1.2	4.0	0.39
Central Hunan			Niutitang	y	19.6		3.4	
				z	5.7			
	XAD1-3	841.9		x	36.7	1.2	5.1	0.41
				y	29.6		4.1	0.42
				z	7.2			
	YC2-17	556.75		x	1637.4	2.6	144.9	1.01
				y	627.2		55.5	
				z	11.3			
NE Chongqing[c]	YC2-42	810.4		x	5160.3	3.7	277.4	1.05
			Shuijingtuo	y	1383.7		74.4	1.08
				z	18.6			
	YC2-65	1050.2		x	6820.3	4.4	245.3	1.23
				y	1541.8		55.5	1.23
				z	27.8			

[a] Ratio of permeability in x-direction to y-direction.

[b] Ratio of horizontal permeability to vertical permeability.

[c] The three shale samples in NE Chongqing exhibit microfracture development.

Table 4. Permeability calculation results using direct solution of N-S equations in Avizo from pore network in Fig.14 and Fig. 15.

Sample ID	Dimensions of FIB-SEM reconstruction for permeability simulation (μm)	Resolution (nm)	Direction	Simulated permeability (nD)	K_x/k_y	$k_{Horizontal}/k_{Vertical}$
XAD 1-2-A	6×6×5.08	10×10×10	x	1569.5	0.8	4.6
			y	1933.1		
			z	338.5		
XAD 1-2-B	6×6×5.98	10×10×10	x	835.3	1.2	1.2
			y	713.4		
			z	670.7		

Author statement

Yong Ma : Conceptualization, Formal analysis, Methodology, Writing – original draft, Writing – review & editing.

Huiting Hu: Methodology, Investigation.

Zhejun Pan: Methodology, Supervision, Writing - Review & Editing.

Ningning Zhong: Supervision, Writing - Review & Editing.

Fujie Jiang: Data Curation, Supervision.

Chengyu Yang: Data Curation, Formal analysis.

Jianbin Ma: Software, Visualization

Binhao Feng: Data curation, Methodology.

Declaration of interests

☒ The authors declare that they have no known competing financial interests or personal relationships that could have appeared to influence the work reported in this paper.

☐ The authors declare the following financial interests/personal relationships which may be considered as potential competing interests: